Rahman, M. M.; Keskinen, K.; Vuorinen, V.; Larmi, M.; Siikonen, T.

Consistently formulated eddy-viscosity coefficient for k-equation model

Published in:
Journal of Turbulence

DOI:
10.1080/14685248.2019.1567926

Published: 01/01/2019

Document Version
Peer-reviewed accepted author manuscript, also known as Final accepted manuscript or Post-print

Published under the following license:
Unspecified

Please cite the original version:
Rahman, M. M., Keskinen, K., Vuorinen, V., Larmi, M., & Siikonen, T. (2019). Consistently formulated eddy-viscosity coefficient for k-equation model. *Journal of Turbulence*, *19*(11-12), 959-994. https://doi.org/10.1080/14685248.2019.1567926

Consistently formulated eddy–viscosity coefficient for k–equation model

*M. M. Rahman[a,b], K. Keskinen[b],V. Vuorinen[b], M. Larmi[b] and T. Siikonen[b]

[a]*Hangzhou Dianzi University, Schoool of Mechanical Engineering, 310018 Hangzhou, China*

[b]*Aalto University, School of Engineering, P.O. Box 14400, FI-00076 AALTO, Finland*

An approach to devising a consistency formulation for P_k/ϵ (production-to-dissipation ratio) is proposed to obtain a non-singular C_μ (coefficient of eddy-viscosity) embedded in the one–equation model based on the turbulent kinetic energy k. The dissipation rate ϵ is evaluated with an algebraically prescribed length scale having only one adjustable coefficient, accompanied by an anisotropic function q_ϵ enhancing the dissipation in non-equilibrium flow regions. The model accounts for the distinct effects of low–Reynolds number (LRN) and wall proximity. The stress–intensity ratio $R_b = \overline{u_1 u_2}/k$ is formulated as a function of local variables without resorting to a constant $\sqrt{C_\mu^*} = 0.3$. The parameters R_b and P_k/ϵ entering the turbulence production P_k prevents presumably the overestimation of P_k in flow regions where non–equilibrium effects could result in a misalignment between turbulent stress and mean strain–rate with a linear eddy–viscosity model. A comparative assessment of the present model with the Spalart–Allmaras (SA) one–equation model and the shear stress transport (SST) k–ω model is provided for well–documented simple and non–equilibrium turbulent flows. Finally, the current model provides a proposal to compute free shear flows.

Keywords: k–equation model, turbulence anisotropy, cubic equation, production-to-dissipation ratio, coefficient of eddy-viscosity.

Nomenclature

C_f	Friction coefficient	Re	Reynolds number
C_p	Pressure coefficient	S	Mean strain–rate tensor
C_μ	Eddy–viscosity coefficient	T_t	Hybrid time–scale
f_μ	Viscous damping function	u_τ	Friction velocity
h	Channel height	W	Mean vorticity
L	Length scale	y^+	$u_\tau y/\nu$
k	Turbulent kinetic energy	ζ	Mean strain-rate/vorticity parameter

*Corresponding author, E-mails: mizanur_rahman@hdu.edu.cn; md.mizan68@gmail.com

δ	Half–channel height; boundary-layer thickness
$\delta_{i,j}$	Kronecker's delta
ϵ	Turbulent dissipation–rate
μ, μ_T	Laminar and turbulent eddy viscosities
$b_{i,j}$	Turbulent anisotropy tensor

Subscript

i, j	Variable numbers

I. Introduction

With relevance to constantly increasing demands on the predictive capability of Reynolds-averaged Navier-Stokes (RANS) formulation, the need for more appropriate evaluations of velocity and length scales has been escalated. Conceptually, both scales can be obtained from the transport equation of turbulent kinetic energy k and the algebraic length–scale determining quantity such as the dissipation ϵ or the specific dissipation ω. The k–equation (one-equation) model proposed by some researchers [1–4] accounts for history effects on the turbulent kinetic energy and is therefore considered an improvement over the algebraic model .[5] However, this model still uses the same ad–hoc assumptions as used in the algebraic model and most researchers have abandoned the k–equation model in the favor of one–equation models based on the transport equations for the eddy viscosity μ_T .[6–14] Nevertheless, it is possible that one can do much better with a single k–equation model in many flows of interest. This would be particularly true if the length scale is governed by an anisotropic feature of the flow. Hence, further study of an improved k–equation model is encouraged .[2–4] A one–equation turbulence model is attractive due to its simplicity of implementation and less demanding computational requirements when compared with the standard two-equation k–ϵ and k–ω models. In addition, a one–equation model includes the transport effect of turbulent kinetic energy and can be considered as a good compromise between algebraic and two–equation models.

In principle, the turbulent kinetic energy transport equation is with the least number of unclosed terms in which ϵ is the only unclosed term having a particular concern. Recently, modified versions of Norris–Reynolds [1] k–equation turbulence model has been proposed by Rahman et al. [2,3] to account for the distinct effects of low–Reynolds number (LRN) and wall proximity. The k and ϵ are evaluated using the k–transport equation in conjunction with the Bradshaw [15] and other empirical relations. The Bradshaw–relation states that the shear stress in the boundary layer is proportional to the turbulent kinetic energy. The eddy–viscosity formulation maintains the positivity of normal Reynolds stresses and preserves the anisotropic characteristics of turbulence in the sense that they are sensitized to rotational and non–equilibrium flows. Xu et al. [4] have also developed a k–equation turbulence model in which ϵ is modeled phenomenologically. The Bradshaw stress–intensity ratio $\left|\overline{u_1 u_2}\right|/k$ is calibrated as a function of controlled local variables. The extension of Bradshaw–relation down to the wall turns out to be of good accuracy, forming a new Reynolds–stress constitutive relation. In particular, the transformation methodology of Menter [8] from the k–ϵ closure to the one–equation model, using the Bradshaw–relation has shown that the use of Bradshaw–relation is quite effective for non–equilibrium flows. Menter [16] has also incorporated the Bradshaw–relation into the k–ω model by introducing a limiter on the eddy–viscosity. The resulting shear–stress transport (SST) model thus partly accounts for the SST effects, having improved results especially for adverse pressure–gradient flows.

Second-order closure models of turbulence, which are based on the Reynolds stress transport (RST) equation, entangle the history and nonlocal effects automatically. Basically, they are formulated to describe complex turbulent flows where there are significant departures from equilibrium .[17] It is worth mentioning that an anisotropic coefficient C_μ augments the capacity of one/two-equation models to account for non-equilibrium effects .[18] With the aid of homogeneous turbulence hypothesis in the limit of equilibrium, Gatski and Speziale (GS) derived an explicit algebraic stress equation for two-dimensional (2D) and three-dimensional (3D) turbulent flows .[19] The GS model utilizes the equilibrium value for P_k/ϵ (production–to–dissipation ratio) arising in the context of the selected pressure–strain model of Speziale, Sarkar and Gatski (SSG) .[20] This may lead the model to inconsistency with a departure from equilibrium. To circumvent this problem, Girimaji [21] developed a fully-explicit, self-consistent variant of the GS model, by solving the cubic equation for C_μ (can be considered also P_k/ϵ) arising in the context of SSG model .[20] Although this achievement yielded a new model variant, the resulting solution for C_μ is unfortunately too cumbersome to be implemented. The purpose of this current work is to extract the proper root of the cubic equation for P_k/ϵ as documented by Jogen and Gatski .[22] The resulting numerical solution to P_k/ϵ is used to obtain an increased predictive performance and robustness characteristics of the GS C_μ.

The newly formulated C_μ is used in conjunction with an improved version of the k–equation model. This version has several desirable attributes relative to the k–equation models developed by Rahman et al. :[2,3] (a) the turbulence structure parameter $R_b = |\overline{u_1 u_2}|/k$ (i.e., Bradshaw-relation) is extended down to the wall with a non–equilibrium function f_k that depends non–linearly on both the rotational and irrotational strains; (b) the production term P_k resulting from a combination of R_b and P_k/ϵ is capable of capturing partially some features of stress–strain misalignment on the evolution of turbulence levels in a linear eddy–viscosity model; (c) the eddy–viscosity formulation resembles the Menter SST k–ω model and (d) the linear/non-linear Reynolds–stress relation can be used to compute Reynolds stresses.

The performance of the new model is demonstrated through comparison with the experimental and DNS data of well–documented wall-bounded flows, namely fully developed channel flows, a flat plate boundary layer flow with zero pressure gradient, a backward facing step flow, an asymmetric plane diffuser flow, flow over a 3D axisymmetric hill, flow past an NACA 4412 airfoil and the flow over an ONERA–M6 wing. These test cases are selected so as to demonstrate the ability of the new k–equation model to replicate the combined effects of LRN, near–wall turbulence and non–equilibrium. Finally, examples of free shear flows such as the free jets are presented followed by the wall-distance-free version of the new model.

II. Proposed k–Equation Turbulence Model

The current objective is to develop a one–equation model which is valid right down to the wall and will be an alternative to the highly empirical–correlation dependent mixing–length model. In collaboration with the RANS equations, the transport equation for the turbulent kinetic energy k is given by:

$$\frac{\partial \rho k}{\partial t} + \frac{\partial \rho u_j k}{\partial x_j} = \frac{\partial}{\partial x_j}\left[\left(\mu + \frac{\mu_T}{\sigma_k}\right)\frac{\partial k}{\partial x_j}\right] + \rho\,\epsilon\left(\frac{P_k}{\epsilon} - 1\right) \tag{1}$$

where ρ is the density, μ implies the molecular viscosity, and the turbulent Prandtl number σ_k connects the diffusivity of k to the eddy–viscosity μ_T. The value of P_k/ϵ is obtained by solving a cubic equation for P_k/ϵ as proposed by Jogen and Gatski .[22] A new formulation for eddy–viscosity coefficient C_μ as suggested by Gatski and Speziale [19] is adopted:

$$C_\mu = \frac{\alpha_1}{1 - \frac{2}{3}\eta^2 + 2\xi^2}; \qquad \eta = \alpha_2\eta_1; \qquad \xi = \alpha_3\eta_2 \tag{2}$$

where $\eta_1 = T_t\,S$, $\eta_2 = T_t\,W$ and T_t is a hybrid time scale. The coefficient C_μ is constructed as a scalar function of the invariants formed by the strain–rate S_{ij} and the vorticity W_{ij} tensors, defined as

$$S_{ij} = \frac{1}{2}\left(\frac{\partial u_i}{\partial x_j} + \frac{\partial u_j}{\partial x_i}\right), \qquad W_{ij} = \frac{1}{2}\left(\frac{\partial u_i}{\partial x_j} - \frac{\partial u_j}{\partial x_i}\right) - C_w\Omega_m e_{mij} \tag{3}$$

where Ω_m is the pure rotation-rate and $C_w = (C_4-4)/(C_4-2)$; the value of C_4 is given latter. In the above equation W_{ij} represents the total vorticity. The invariants of mean strain–rate and vorticity tensors are given by $S = \sqrt{2S_{ij}S_{ij}}$ and $W = \sqrt{2W_{ij}W_{ij}}$, respectively. The associated coefficients $(\alpha_1 - \alpha_3)$ are given by

$$\begin{aligned} \alpha_1 &= g\left(\frac{1}{4} + \frac{2}{3}\sqrt{\Pi_b}\right), & \alpha_2 &= \frac{3}{8\sqrt{2}}\,g \\ \alpha_3 &= \frac{3}{\sqrt{2}}\,\alpha_2, & g &= \left(1 + 2\,\frac{P_k}{\epsilon}\right)^{-1} \end{aligned} \tag{4}$$

where $\Pi_b = b_{ij}b_{ij}$; the anisotropy of the Reynolds stress b_{ij} is defined as

$$b_{ij} = \frac{\overline{u_i u_j}}{2k} - \frac{1}{3}\,\delta_{ij} \tag{5}$$

and $\sqrt{\Pi_b}$ in Eq.(4) can be modeled as :[22,23]

$$\sqrt{\Pi_b} \approx \frac{P_k}{\epsilon}\,\zeta^{-1}; \qquad \zeta = T_t S\ \max(1, \Re) \tag{6}$$

where $\Re = |W/S|$ is a dimensionless parameter which is very useful in characterizing the flow. For instance, for a pure shear flow $\Re = 1$, whereas for a plane strain flow $\Re = 0$. It should be noted that the shear and vorticity parameters η_1 and η_2, respectively in C_μ can improve the prediction of both the shear and vorticity dominated flows that are far from equilibrium.

In an LRN one–equation model, the k–equation is solved by assigning $k = 0$ on the solid boundary. The k–equation turbulence model is proposed to account for the distinct effects of LRN and wall proximity. To invoke this phenomenon, the eddy viscosity μ_T is formulated as

$$\mu_T = f_\mu C_\mu \rho\, k\, T_t \tag{7}$$

Since the viscous dissipation dominates near a wall, therefore the use of a dynamic time scale k/ϵ is not appropriate in the near–wall region. To address this issue, the Kolmogorov time scale $\sqrt{\nu/\epsilon}$ is used as a lower bound:

$$T_t = \max\left(\frac{k}{\epsilon};\ C_T\sqrt{\frac{\nu}{\epsilon}}\right) \tag{8}$$

In k–ϵ models, this approach prevents the singularity in the dissipation equation down to the wall. Equation (8) ensures that the eddy time scale never falls below the Kolmogorov time scale $C_T\sqrt{\nu/\epsilon}$, which would be dominant in the immediate neighborhood of the solid wall. The empirical constant $C_T = \sqrt{2}$ associated with the Kolmogorov time scale is estimated from the behavior of k in the viscous sublayer .[24]

The primary objective of introducing an eddy–viscosity damping functionf_μ with turbulence models is to represent the kinematic blocking by the wall. The eddy–viscosity damping function included in Eq. (7) is devised as

$$f_\mu = tanh\left(\frac{A_\mu Re_y}{20}\right)\left(1 + \frac{2\zeta}{Re_y^{3/2}}\right) \tag{9}$$

where $A_\mu = C_\mu\,\zeta$ and $Re_y = \sqrt{k}y/\nu$ denotes the turbulent Reynolds number and the kinematic viscosity $\nu = \mu/\rho$.

The dissipation of turbulent kinetic energy ϵ plays an important role in determining the time scale T_t. Instead of solving the dissipation ϵ–equation, ϵ near the wall is determined using k and a length scale as:

$$\epsilon = A_\epsilon \frac{k^{3/2}}{y}, \qquad A_\epsilon = \max\left(0.25; \frac{C_\mu^{3/4}}{\kappa}\right) \tag{10}$$

where $\kappa = 0.41$ is used herein; although a range of values for $\kappa = 0.34$–0.46 is available .[25] As shown in Fig. 1, the profiles of parameter A_ϵ follow the similar trends for fully developed channel flows [27] at $Re_\tau = 180$ and 395, respectively. This formula matches the channel flow and flat–plate boundary layer at several Reynolds numbers quite well, especially near the wall. However, the formulation may deteriorate the model performance wherein the excessive flow inhomogeneity exists (i.e., flow separation and reattachment). In the current study, Eq. (10) is reconstructed as:

$$\epsilon = A_\epsilon \frac{k^{3/2}}{L}, \qquad A_\epsilon = \max\left(0.25 + q_\epsilon; \frac{C_\mu^{3/4}}{\kappa}\right) \tag{11}$$

It is well-known that in the boundary layer (BL), the inner-log layer scales properly when using the wall distance y as a length scale. However, in the wake region of the BL, the eddy-viscosity scales with the BL thickness (δ). Note that all historically accepted k-based one-equation models use a length scale which is $L = \min(c_1 y, c_2\delta)$ (where c_1 and c_2 are constants) to resolve this issue. To simply avoid the δ-part is clearly a violation of basic BL modeling concepts. To account for this phenomenon in the present simple mixing-length model, the length scale L must be associated with the wall-distance and viscous based scalings; they are designed as

$$\frac{1}{L_{wd}} = \frac{1}{y}, \qquad \frac{1}{L_{vis}} = C_\mu^*\sqrt{1 + \frac{\chi}{C_T}}\sqrt{\frac{\rho S}{\mu + \mu_T}} \tag{12}$$

where $\chi = \mu_T/\mu$ and $C_\mu^* = 0.09$. The behaviors of length scales are presented in Fig. 2 using DNS data for fully developed channel flows [27] at $Re_\tau = 180$ and 395, respectively. It seems likely that the wall-distance dependent length scale L_{wd} plays the role in the vicinity of the inner-log layer; the viscous length scale L_{vis} is activated afterwords. To enhance numerical stability, the parameter L is implemented as follows:

$$\frac{1}{L} = \begin{cases} \dfrac{1}{L_{wd}} & \text{if} \quad Re_y \leq 60 \\ \min\left[\dfrac{1.5}{L_{wd}}; \max\left(\dfrac{1}{L_{wd}}; \dfrac{1}{L_{vis}}\right)\right] & \text{otherwise} \end{cases} \tag{13}$$

Noteworthily, $Re_y = 60$ is equivalent to $y^+ \approx 30$ (i.e., known as viscosity affected regions) as determined from the DNS data for fully developed channel flows .[27]

The function q_ϵ in Eq. (11) is constructed such as to preserve the anisotropic characteristics of turbulence encountered in rotational and non-equilibrium flows; it is formulated as:

$$q_\epsilon = \begin{cases} \dfrac{\sqrt{|1-\Re^2|}}{C_T \max(1;\Re)} & \text{if} \quad \Re \neq 0 \\ 0 & \text{otherwise} \end{cases} \tag{14}$$

Intuitively, q_ϵ amplifies the level of dissipation in non-equilibrium flow regions, thus reducing the kinetic energy and length scale magnitudes to improve prediction of adverse pressure gradient flows, involving flow separation and reattachment.

A new stress–intensity relationship can be deduced from the Bradshaw hypothesis ,[15] which has been implemented in many turbulence models to evaluate secondary viscosity and production terms. Using the curve–fitting formula of She et al. ,[26] the ratio $b_{12} = \left|\overline{u_1 u_2}\right| / k$ can be obtained as:

$$b_{12} = \frac{\left|\overline{u_1 u_2}\right|}{k} = R_b = \min\left[\sqrt{C_\mu^*}; \frac{C_\mu^*}{5} \frac{Re_y^{0.6}\left(1+\dfrac{C_\mu^*}{110}Re_y\right)^{0.4}}{\sqrt{1+\left(\dfrac{C_\mu^*}{18}Re_y\right)^2}}\right] \tag{15}$$

where R_b can be regarded as a measurement of wall constraint on the correlation between streamwise and wall–normal fluctuations, approaching a constant value away from the wall. The performance of Eq. (15) is tested by using the DNS data from fully developed channel flows [27] at $Re_\tau = 180$ and 395 as shown in Fig. 3.

The principle shear stress can be obtained from Eq. (15) as

$$\left|\overline{u_1 u_2}\right| = R_b\, k = \frac{\mu_T}{\rho}\, S \tag{16}$$

and the turbulent kinetic energy production can be redefined as $P_k = k\, R_b\, S$. It is worth mentioning that the stress–intensity ratio R_b resembles the stress–strain misalignment parameter C_{bs} of the k–ϵ–C_{bs} model, where C_{bs} is determined from a transport equation.[28] Finally, the introduction of R_b and P_k/ϵ into the k–equation model requires only a single modification to the transport equation for turbulent kinetic energy:

$$\frac{\partial \rho k}{\partial t} + \frac{\partial \rho u_j k}{\partial x_j} = \frac{\partial}{\partial x_j}\left[\left(\mu + \frac{\mu_T}{\sigma_k}\right)\frac{\partial k}{\partial x_j}\right] + \rho\, P_k - \rho\, \epsilon \tag{17}$$

where $\sigma_k = 1.0$, $P_k = \min\left[f_\mu\left(\frac{P_k}{\epsilon}\right)\epsilon;\, k\, R_b\, S\right]$ and $\mu_T = f_\mu \rho k T_t \min\left(C\mu;\, \frac{R_b}{f_\mu \zeta}\right)$; ϵ and R_b are given by Eqs. (11) and (15), respectively. Note that the modification in μ_T avoids the non–physical behavior due to the inappropriate modeling of principal turbulent shear stress introduced by the eddy–viscosity concept especially in strong pressure-gradient regions where the production of turbulent kinetic energy is larger than its dissipation-rate. It seems likely that the current model bears a close resemblance to the Menter SST k–ω model .[16]

III. Production–to–Dissipation Rate: P_k/ϵ

A single equation accounting for an algebraic relationship among three state variables (P_k/ϵ: turbulent production-to-dissipation rate ratio; η_1: strain-rate parameter; $\Re$: ratio of mean rotation-rare and strain-rate invariants) is derived by Jogen and Gatski [22] as:

$$\left(\frac{P_k}{\epsilon}\right)^3 + A\left(\frac{P_k}{\epsilon}\right)^2 + B\left(\frac{P_k}{\epsilon}\right) + C = 0 \tag{18}$$

where the numerical coefficients are given by

$$A = \frac{2\beta}{\alpha};\quad B = -\frac{1}{\alpha^2}\left[\alpha a_1 \eta_1^2 + \eta_1^2\left(\frac{1}{3}a_3^2 - a_2^2\Re^2\right) - \beta^2\right];\quad C = -\frac{\beta a_1 \eta_1^2}{\alpha^2} \tag{19}$$

With the aid of pressure-strain correlation model of SSG ,[20] the associated constants are given by

$$\begin{aligned}
\alpha &= \frac{C_1^1}{2} + 1; & \beta &= \frac{C_1^0}{2} - 1\\
a_1 &= \frac{2}{3} - \frac{C_2}{2}; & a_2 &= 1 - \frac{C_4}{2}\\
a_3 &= 1 - \frac{C_3}{2}; & C_1^0 &= 3.4\\
C_1^1 &= 1.8; & C_2 &= 0.36\\
C_3 &= 1.25; & C_4 &= 0.40
\end{aligned} \tag{20}$$

Using the constants of Eq. (20) in Eq. (19) yields:

$$A \approx \frac{3}{4};\quad B \approx -0.136\left[2\eta_1^2\left(1 - \frac{2}{3}\Re^2\right) - 1\right];\quad C \approx -0.1\eta_1^2 \tag{21}$$

The solution to the cubic Eq. (18) can be made using the standard procedure described in most mathematical handbooks. Define the following:

$$Q = \frac{3B - A^2}{9};\quad R = \frac{9AB - 27C - 2A^3}{54};\quad D = Q^3 + R^2 \tag{22}$$

where D is called the discriminant. If $D > 0$, the cubic Eq. (18) has one real and two complex conjugate roots. The choice of P_k/ϵ is obvious and the one with the real part can be computed as:

$$\left(\frac{P_k}{\epsilon}\right)_1 = -\frac{A}{3} + \left(R + \sqrt{D}\right)^{1/3} + \left(R - \sqrt{D}\right)^{1/3} \tag{23}$$

When $D < 0$ Eq. (18) has three real and unequal roots given by:

$$\begin{aligned}
\theta &= \frac{1}{3} arccos \left(\frac{R}{\sqrt{-Q^3}} \right) \\
\left(\frac{P_k}{\epsilon} \right)_1 &= -\frac{A}{3} + 2\sqrt{-Q}\ cos\theta \\
\left(\frac{P_k}{\epsilon} \right)_2 &= -\frac{A}{3} - 2\sqrt{-Q}\ cos \left(\frac{\pi}{3} - \theta \right) \\
\left(\frac{P_k}{\epsilon} \right)_3 &= -\frac{A}{3} - 2\sqrt{-Q}\ cos \left(\frac{\pi}{3} + \theta \right)
\end{aligned} \tag{24}$$

Obviously, the only physically viable root in Eq. (24) is $(P_k/\epsilon)_1$. A value of $D = 0$ yields:

$$-Q = R^{2/3} \tag{25}$$

This signifies that $\theta = 0$; $cos(\theta) = 1$ and the magnitudes of $(P_k/\epsilon)_1$ in both Eqs. (23) and (24) are identical. Therefore, the branch of solution that will lead (P_k/ϵ) to as a continuous function of the discriminant D is:

$$\frac{P_k}{\epsilon} = \begin{cases} -\frac{A}{3} + \left(R + \sqrt{D} \right)^{1/3} + \left(R - \sqrt{D} \right)^{1/3} & \text{if} \quad D > 0 \\ -\frac{A}{3} + 2\sqrt{-Q}\ cos\theta & \text{if} \quad D \leq 0 \end{cases} \tag{26}$$

Noteworthily, at $\eta_1 = \eta_2 = 0$; $D < 0$ and $2\sqrt{-Q}\ cos\theta \approx A/3$. Therefore, $(P_k/\epsilon) \approx 0$.

Figure 4 illustrates the distribution of (P_k/ϵ) as a function of shear parameter ζ ($\Re = 1$). As is evident, the relation (26) recovers the self-consistent model of Girimaji [21] for the weak equilibrium condition. Figure 5 shows the profiles of C_μ as a function of ζ. Conspicuously, the C_μ–distribution is in excellent agreement with various DNS data .[29–31] The proposed C_μ is reduced significantly with increasing ζ and maintained at a level that could mimic the complex turbulent flows.

Using the DNS data [27] for fully developed turbulent channel flows, plots of $C_\mu f_\mu$ are shown in Fig. 6 and a good correlation is obtained. Evidently, the adopted form of $C_\mu f_\mu$ converges to replicate the influences of LRN and wall proximity. The empirical function f_μ is valid in the whole flow field, including the viscous sublayer and the logarithmic layer.

Using Boussinesq approximation the Reynolds shear-stress anisotropy in homogeneous shear flow can be given as:

$$b_{12} = -\frac{C_\mu}{2}\zeta \tag{27}$$

Detailed comparisons of the anisotropies with the DNS and experimental data are shown in Table 1 for the channel flow of Kim [32] in the inertial sublayer at $\zeta = 3.3$, and in Table 2 for the homogeneous shear flow of Tavoularis and Corrsin [33] at $\zeta = 6.0$, respectively. Clearly, the present model provides reasonable anisotropy of Reynolds stresses for both the boundary layer and homogeneous shear flows, compared to the standard $k - \epsilon$ eddy-viscosity model with $C_\mu = 0.09$. Therefore, the current model is capable of predicting the turbulent driven secondary flows.

IV. Computed Flow Fields

To validate the newly proposed k–equation model, a few applications to one/two/three–dimensional turbulent flows consisting of fully developed channel flows, a flat plate boundary layer flow with zero pressure gradient, a backward facing step flow, an asymmetric plane diffuser flow, flow over a 3D axisymmetric hill, flow past an NACA 4412 airfoil, the flow over an ONERA–M6 wing and free shear flows (i.e. plane and round jets) are considered. To evaluate the model reliability and accuracy, the present model predictions are compared with those from the widely used SA model [7] and Menter's SST (shear–stress transport) k–ω [16] model. It should be noted that compared to the SA and SST models, the new model has additional anisotropic coefficients depending non-linearly on both the rotational and irrotational strains.

A cell centered finite-volume scheme combined with an artificial compressibility approach is employed to solve the flow equations .[34–36] A fully upwinded second-order spatial differencing is applied to approximate the convective terms. Roe's [37] damping term is used to calculate the flux on the cell face. A diagonally dominant alternating direction implicit (DDADI) time integration method [38] is applied for the iterative solution to the discretized equations. A multigrid method is used for the acceleration of convergence .[39] The basic implementation of the artificial compressibility method and other aspects of the numerical scheme are described elsewhere .[34–36] A variable grid spacing is used to resolve the sharp gradient in near-wall regions. Grid densities are varied to ensure the grid independence of the numerical results.

IV.A. Channel flow

The computation is carried out for fully developed turbulent channel flows at $Re_\tau = 180$ and 395 for which turbulence quantities are available from the DNS data [27] . The calculation is conducted in the half–width of the channel, using the one–dimensional RANS solver. Figure 7 shows the mean velocity distributions using the present turbulence model on three grids. No appreciable differences are observed between the coarse grid (1×64) and fine grid (1×70) results. Therefore, a 1×64 nonuniform grid is used across the channel half-width which is sufficient to ensure a grid independent numerical solution. To ensure the resolution of the viscous sublayer, the first grid node near the wall is placed at $y^+ \approx 0.3$. Comparisons are made by plotting the results in the form of $u^+ = u/u_\tau$, $k^+ = k/u_\tau^2$, $\overline{uv}^+ = \overline{uv}/u_\tau^2$ and $\epsilon^+ = \nu\epsilon/u_\tau^4$ versus y^+.

Figure 8 shows the velocity profiles obtained using different models. Predictions of the present, SA and SST models agree well with the DNS data. Noteworthily, although not having the transport and diffusion effects of the dissipation-rate, there is reasonable agreement of the present model with the DNS data. Profiles of turbulent shear stresses are shown in Fig. 9. Agreement of predictions from the present, SA and SST models with the DNS data is fairly good. It can be seen that the present and SST models give superior predictions in the near-wall region compared to the SA model.

Further examination of the model performances are shown by the k^+ profiles in Fig. 10. It can be seen that k^+ is somewhat over-predicted in the outer layer especially at $Re_\tau = 180$; however agreeing well with the DNS in the near-wall region. The SST model badly under-predicts the k^+ profiles near the wall. Figure 11 exhibits the profile of ϵ^+ from the present and SST computations. For the SST model $\epsilon^+ = C_\mu^* k^+ \omega^+$. None of them cannot capture a maximum ϵ^+ close to the wall in line with the experimental and DNS data. however, both the models predict the ϵ^+ profiles qualitatively well after the wall-region. Such a behavior of the ϵ^+-profile in near-wall regions may strengthen the numerical stability, thereby enhancing the convergence of the numerical solver as is experienced by the SST model. The profiles of production-to-dissipation ratio $P_k/\epsilon = \min\left[f_\mu\left(\frac{P_k}{\epsilon}\right); R_b\, S\, T_t\right]$ for the present model as well as for the SST model are shown in Fig. 12 and a better correspondence with the DNS data is obtained by the present model than those of the SST model. Undoubtedly, the limiting-influence of Eq.(11) is manifested in the P_k/ϵ-profile of the current model.

IV.B. Flat-plate boundary layer flow

The performance of the proposed model is further contrasted with the experimental data of the flow over a flat plate with a high free stream turbulence intensity known as T3B. The test case is taken from "ERCOFTAC" Fluid Dynamics Database WWW Services (http://fluindigo. mech.surrey.ac.uk/) preserved by P. Voke. Measurements down to $x = 1.495\ m$ which corresponds to $Re_x \approx 94000$, are made by J. Coupland at Rolls-Royce. The inlet velocity is 9.4 m/s and the pressure gradient is zero. The upstream turbulence intensity $Tu = 6.0\ \%$, defined as $Tu = \sqrt{\frac{2}{3}k}/U_{ref}$, where U_{ref} indicates the reference velocity; it drives a quick transition. The turbulent to laminar viscosity ratio $\mu_T/\mu = 1$ is prescribed at the inlet.

Computations begin 16 cm ahead of the leading edge and symmetric conditions are applied. The length and height of the grid are 1.6 m and 0.3 m, respectively. The near-wall grid node is located at $y^+ < 1.0$, except the point at the leading edge ($y^+ = 2.1$). The grid size is 96×64 and heavily clustered near the wall. Figure 13 shows the skin-friction profiles wherein two different grid resolutions are provided for the present model. It appears to be nearly grid converged on two-grid levels. Therefore, the fine 96×64 non-uniform grid is sufficient to ensure a grid independent numerical solution.

The predicted skin friction coefficients ($C_f = 2u_\tau^2/U_{ref}^2$) are compared with the experimental data in Fig. 14. It can be seen that the present model prediction matches measurements very well, especially in the fully developed regions. A clear laminar region reveals the potential of the present model in capturing the transition. The overall performance in predicting the friction coefficient is the best for the SA model, exhibiting an interesting feature that the transition starts at the right position and it is strong enough. In contrast, the SST model provides earlier transition than that seen in the experiment and it is too weak. Seemingly, the agreement between the computations and the experiment is fairly good toward the end of the transition (e.g., beyond $x = 0.195m$). However, predictions of SA and SST models are somewhat on a lower level than the data show.

Figure 15 presents a comparison of all three models against experimental mean velocity profiles at three representative positions. The present model predicts the correct velocity profiles and surprisingly, the weak regions are well described. Conspicuously, the distinct nature of predicted friction coefficients in Fig. 14 can explain the differences among them (i.e., velocity profiles) in the outer layer. Comparisons of other indicative plots, namely turbulent shear stress, kinetic energy and dissipation-rate are presented in Figs. 16, 17 and 18, respectively with experimental data at the same positions. Note that the $\overline{ww}$ component is not measured in the experiment, the usual approximation $k \approx 3/4(\overline{uu} + \overline{vv})$ is employed. As is clearly noticed, the agreement among the shear stress profiles is somehow good. However, the SST model under-predicts the turbulent energy and over-estimates the turbulent dissipation ($\epsilon^+ = C_\mu^* k^+ \omega^+$) in the near-wall region compared to the present model.

IV.C. Backward facing step flow

The flow over a backward facing step is one classic complex case for the test of flow with separation and reattachment. The computations are conducted corresponding to the experimental case with a zero-deflection of the wall opposite to the step, as investigated by Driver and Seegmiller .[40] The reference velocity $U_{ref} = 44.2\ m/s$ and the step height $h = 0.0127\ m$. The ratio between the channel height and the step height is 9, and the step height Reynolds number is $Re = 37500$. At the channel inlet, the Reynolds number based on the momentum thickness is $Re_\theta = 5000$.

For the computations, grids are arranged in two blocks. The smaller one (extended from the inlet to the step) contains a 16×48 non-uniform grid and the grid size for other one is 120×80. The near-wall grid node is placed approximately at $y^+ < 1.0$. The inlet conditions are specified four step heights upstream of the step corner and the outlet boundary conditions are imposed 30 step heights downstream of the step corner. The inlet profiles for all dependent variables are generated by solving the models at the appropriate momentum thickness Reynolds number. Profiles of mean velocity, shear stress, turbulent kinetic energy and dissipation-rate at the inlet are shown in Fig. 19. All models match the experimental data well; the dissipation-rate profile of the present model is almost analogous to that of the SST model. All the quantities shown below are normalized by the step height h and the experimental reference free stream velocity U_{ref}, provided that the distance x/h is measured exactly from the step corner. Figure 20 shows the skin-friction coefficient using the present turbulence model on two grids (only the big computational block is shown). Except outside the separated flow region, there is little difference between the coarse 60×40 and fine grid 120×80 results. Other turbulence models show similar/smaller grid sensitivities. Therefore, computations involving a 120×80 non-uniform grid resolution are considered to be accurate to describe the flow characteristics.

Computed and experimental friction coefficients C_f along the bottom wall (step side wall) are plotted in Fig. 21 . As is observed, the present model fits the measurements very well in the recirculation region but under-estimates the recovery region; this is an issue for the future study. The SA and SST models predict the skin-friction coefficients qualitatively. The positive C_f that starts from $x/h = 0$, is due to a secondary eddy which sits in the corner at the base of the step, inside the main recirculation region. The recirculation length predicted by each model can be determined by measuring the distance from the step corner to a point at which the curve changes sign. The present model predicts a recirculation length of 6.6, and the corresponding predictions by the SA and SST models are 6.0 and 6.4. The experimental value of the reattachment length is 6.26 ± 0.1, making a fairly good correspondence with all models.

The streamwise mean velocity profiles at three representative positions are depicted in Fig. 22. Obviously, the predictions of all models are in good agreement with the experiment. Comparisons are extended to the distributions of the Reynolds shear stress and the corresponding turbulent kinetic energy at different x/h locations behind the step corner, as shown in Figs. 23 and 24. Since the $\overline{ww}$ component is not measured in the experiment, the usual approximation $k \approx 3/4(\overline{uu} + \overline{vv})$ is employed. A closer inspection of the distribution indicates that for the shear stress in Fig. 23, the present and SST model predictions are in a broad agreement with the experimental data. As can be seen in Fig. 24, the SST model performs well in reproducing the experimental trend. However, the peaks of k are over-predicted by the present model compared to the measurements. It is a bit nebulous that the inaccurate prediction of the k-distribution by the present model has little effect on the C_f, u and uv profiles. It seems likely that for a non-linear eddy-viscosity model, this is a common feature of turbulent flows with separation and reattachment .[41] Dissipation-rate profiles are plotted in Fig. 25. As expected, the present model predictions follow the analogous distribution of k. However, the magnitude of dissipation-rate with the SST model is very large in the vicinity of the wall; this is why, the SST model probably fits the k-profile with the experiments.

IV.D. Asymmetric plane diffuser flow

To validate the performance in complex separated and reattaching turbulent flows, the present model is further applied to the flow in an asymmetric diffuser with an opening angle of 10^o, for which measurements are available .[42] The expansion ratio of 4.7 is sufficient to produce a separation bubble on the deflected wall. Hence the configuration provides a test case for smooth and adverse pressure-driven separation. The entrance to the diffuser consists of a plane channel to invoke fully developed flow with $Re = 2.0 \times 10^4$ based on the centerline velocity U_{ref} and the inlet channel height h. The length of the computational domain is $76h$. Grid independent computations are performed on a 120×72 non-uniform grid resolution. The thickness of the first cell remains below one in y^+ unit on both the deflected and flat walls. The computational grid is displayed in Fig 26. Profiles of mean velocity, shear stress, turbulent kinetic energy and dissipation-rate at the inlet are presented in Fig. 27. All models ensure close adherence to the experimental data. The dissipation-rate is over-estimated by the SST model compared to the present model. Figure 28 shows the skin-friction coefficient using the present turbulence model on two grids. Notably, the existing unusual behavior with the C_f-profiles in the beginning of recirculation is probably due to Eq. (11). As can be seen, there is very little difference between the coarse (60×36) and fine grid (120×72) results. Therefore, computations involving a 120×72 non-uniform grid resolution are considered to be accurate to describe the flow characteristics.

Figures 29 and 30 show the predicted skin-friction coefficients. The results of the present and SA models are in reasonable agreement with the SST model and measurements. In Fig. 29, after $x/h = 25$ the SST presents a better behavior; the modification to the shear-stress transport in the eddy-viscosity formulation (limited to wall bounded flows) is perhaps responsible for this enhancement. It can be seen that the present model predicts the C_f-profile (along the straight top wall) better than the SA model. Figure 31 exhibits the mean velocity profiles at four representative locations in the diffuser. The performance of the present model in predicting the velocity profiles is distinguishable. Unlike the SA model, the present model employs the non-linear formulation for turbulent eddy-viscosity, and hence yields results in better agreement with the data. Remarkably, the SST model over-predicts the peak of u-profile toward the outlet of the diffuser, for instance, $x/h = 30$; apparently, the accurate prediction of C_f-distribution by the SST model after $x/h = 25$ has little effect on the evaluation of u-profiles. However, other two models give reasonable predictions.

Comparisons of the Reynolds shear stress and turbulent kinetic energy at different x/h locations are displayed in Figs. 32 and 33, respectively. Since the $\overline{ww}$ component is not measured in the experiment, the usual approximation for $k \approx 3/4(\overline{uu} + \overline{vv})$ is employed. Results indicate that the present and SA models under-predict the shear stresses at $x/h = 14$, 20 and 30, contrary to what the data show. However, the k–profiles predicted by the present model has comparable agreement with the experimental data. The SST model acceptably predicts the measured data for u (except after $x/h = 25$), uv and k profiles; this is expected since it solves the transport equations with the shear-stress modification. The dissipation-rate distributions are illustrated in Fig. 34. Noticeably, the profiles are dissimilar to those of the backward facing step flow; the flow mechanism is a bit different. In fact, many RANS model predicts the step flow case fairly, however fails in capturing the features of the diffuser case due to the inaccurate prediction of the dissipation-rate. Evidently, the SST model offers large magnitudes of the dissipation-rate in the near-wall vicinity compared to the present model. This aspect probably provides better predictive capabilities of the SST model when compared to using viscous wall-damping functions in wall-bounded flows.

IV.E. Three-dimensional axisymmetric hill

The flow over an axisymmetric three-dimensional (3D) hill is characterized by 3D separation on the leeside of the hill. The experiment was conducted by Simpson et al.[43] at Virginia Polytechnic Institute and State University. This case was chosen as a test case at the *11th ERCOFTAC Workshop on Refined Turbulence Modeling* (Gothenburg, Sweden, 7–8 April 2005). The results presented at the workshop indicate that this flow is a rather challenging type for modeling 3D turbulent separation and simulating downstream flow properties. RANS turbulence models in general give rise to largely erroneous predictions of the flow, particularly in the region over the leeside of the 3D hill and downstream thereafter.

The geometry is an axisymmetric hill with a height $h = 78\ mm$ and a radius of the circular base $a = 2h$. The shape is defined by Bessel functions. The Reynolds number based on the height h and a nominal free-stream velocity $U_{ref} = 27.5\ m/s$ is $Re = 1.3 \times 10^5$. The thickness of the boundary layer at 2 hill-heights upstream of the hill is approximately $0.5h$. The mean flow is closely symmetric about the centerline and complex vortical separations occur on the leeside that merge into two large streamwise vortices downstream. The flow along the streamwise centerline at $x/h = 0.39$ is a downwashing reattachment flow and only one mean vortex exists on each side of the centerline.[43] Therefore, half of the computational domain is considered which has dimensions of $L_x \times L_y \times L_z = (-x_0 + 15.7)h \times 3.2h \times 5.85h$. The inflow section is located at $x_0 = -4.11h$ upstream from the center of the hill, where the origin of the coordinate system is set. The computational grid in the symmetry plane z/h = 0 for 3D hill flow is portrayed in Fig. 35. Interpolated profiles of mean velocity, shear stress and turbulent kinetic energy from measured data at $x = 0$ with the hill removed are prescribed at inflow section at $x_0 = -4.11h$. Inlet profiles are presented in Fig. 36. All models ensure good agreement with data. No experimental data are available for the dissipation-rate. Symmetric conditions are imposed on the spanwise side boundaries. Figure 37 shows the skin-friction coefficient using the present turbulence model on two grids. As is seen, the agreement between the coarse $(80 \times 40 \times 32)$ and fine grid $(160 \times 80 \times 64)$ is better in the recovery region rather than in the recirculation region; obviously, the differences are small. Therefore, Computations involving a $160 \times 80 \times 64$ (in x, y and z directions, respectively) nonuniform grid resolution are considered to be accurate to describe the flow characteristics.

Not shown, computational velocity vector fields at the symmetry plane $z/h = 0$, drawn from all models produce the streamwise extension of separation bubbles that is more/less similar to the measured velocity field, while the predicted thickness of the bubbles seems somewhat larger than the measured schematic. Figure 38 shows the skin -friction coefficients along the 3D hill surface at the center-plane, from which recirculation lengths formed by all models can be evaluated. The recirculation regions predicted by the present, SA and SST models are $0.44 \leq x/h \leq 2.35$, and $0.44 \leq x/h \leq 2.4$ and $0.3 \leq x/h \leq 2.7$, respectively. According to the experiment, the flow in the symmetry plane separates about 1 hill height ($x/h = 0.96$) after passing over the hill crest. The separation zone is very shallow and the flow reattaches at the foot of the hill at $x/h = 2$. The present model makes somewhat better correspondence with the experimental separation length, particularly the shallow-feature than that of SA/SST. The present model outperforms the other two models in this particular case, regarding the separation length. The SST model returns the most exaggerated separation length.

As is observed form Fig. 38, the differences between the predictions and experiment reflect the much more intense reverse flow predicted by all models in the leeward central portion of the hill surface and the absence of the downwash described above. They are also consistent with the much faster experimental pressure recovery behind the hill, relative to the plateaus in the simulations, shown in Fig. 39 and characteristic of massive separation. It seems that all models predict the pressure-coefficient C_p distributions reasonably well. However, Fig. 22, in particular, reveals that the inflexion in the C_p curves, associated with the weak separation on the leeside of the hill is well captured by the present and SA models.

To examine the wake statistics, streamwise velocity profiles at various spanwise locations on the plane $x/h = 3.69$ are shown in Fig. 40. The vertical distributions measured at four stations have been used for comparisons, taken respectively at $z/h = 0$, $z/h = -0.33$, $z/h = -1.30$ and $z/h = -1.79$. Consistent with the earlier results, the excessively large separation zone, returned by all models produces a too slow recovery of the flow in the wake, so that the streamwise velocity is underpredicted. However, at other side stations namely $x/h(-1.30, -1.79)$, these velocities are more sensibly overpredicted in the boundary layer. It seems likely that the present model predictions are analogous to those of the SA model.

Consistent with the differences in the mean flow, the computed turbulence kinetic energy, shown in Fig. 41, decreases rapidly in the spanwise direction, confirming that the wake is confined to a much narrower region around the center-plane than its experimental counterpart. However, the predicted turbulence energy by both the present and SST models agrees reasonably well with the measured data at stations $x/h(-1.30, -1.79)$. However, at other stations, the present/SST model at least mimic the experimental k trends. Figure 42 compares the dissipation-rate profiles between the present and SST models. At stations $x/h(-1.30, -1.79)$, the present model returns the closest behavior to the SST model in the boundary layer. However, the distributions differ from each other at other two stations (complex wake region, seen from the experiment) since the present model does not solve the transport equation for the dissipation-rate. To this end, it must be stressed that the present model shows a slight superiority over the SST model in predicting especially C_f, C_p and u profiles for this test case, an improvement that is deemed to be due to the use of an anisotropic algebraic formulation for the dissipation-rate.

IV.F. Flow past an NACA 4412 airfoil

This flow case with a high angle of attack (AOF) induces external flow separation under adverse pressure gradient, which has a strong impact on overall pressure distributions. The present model is validated against the experiment of Coles and Wadcock.[44] Performances of SA and SST models for this test case are well-known[45] and therefore, they are excluded. An AOF = 13.87^o with a freestream velocity of $U_{ref} = 27.13\ m/s$ generates a trailing-edge separation (with a shallow bubble) on the upper surface of airfoil. This case has a Mach number of $M = 0.09$ and Reynolds number $Re = 1.52 \times 10^6$ based on a chord length of $c = 1$. A non–uniform C–type grid 896×256 is used with 512 nodes lying on the airfoil surface. The outer boundaries around the airfoil are set to 50 chord lengths and the maximum height of the first near-wall grid node is at $y^+ < 1.0$.

The mean pressure coefficient for airfoil is depicted in Fig. 43. As can be seen, considerable discrepancy between predicted and measured pressure coefficients on the upper surface is distinguishable, particularly in the separation region. In fact, other widely used turbulence models[45] (i.e., SA and SST models) provide the similar picture of pressure distribution. Figure 44 compares the mean streamwise velocity profiles as predicted by the present model against measurements at six locations on the suction side of airfoil. Present model predictions maintain good agreement with experimental data before and after the separation, yielding a clear evidence that the new model may handle adverse pressure gradient flows well. However, compared with experiments slight deviations are observed and recalling the performance of traditional models, the present model has the potential in predicting the shallow separation. Remarkably, the current model captures the shallow feature of separation region associated with the 3D axisymmetric hill flow, although it is not consistently perfect with experimental data.

IV.G. ONERA–M6 wing

The ONERA–M6 wing is a widely used three–dimensional test case for validation of numerical methods and turbulence models for transonic flows. The flow–field is computed at a free-stream Mach number of 0.8395, an angle of attack 3.06^o, and the free-stream Reynolds number $Re = 11.71 \times 10^6$. A structured grid used in the simulation consists of four blocks with $1,572,864$ cells and the minimum normalized grid spacing to the wall is 2×10^{-5}. The main feature of this test case is described as the interactions of shock–wave and boundary–layer, and the separation induced by the strong shock (i.e., shock induced boundary–layer separation). However, the current study focuses on the validation of the turbulence models based only on available experimental data for pressure coefficients at various spanwise sections of the wing .[46]

The pressure coefficient results are compared over the wing sections located at $y/b = 20$, 44, 65, 80, 90 and 95% half–span in Fig. 45. It can be observed that all models match the experiment very well. Slight over–predictions appear near the leading edge on the upper wing surface, but they are very minor. In addition, the pressures on the lower side of the wing as well as those at the trailing edge are well predicted and the overall profiles are captured very well by all models. The difference in the pressure distributions between the present and SA models is not significant. Nevertheless, the SST computations differ slightly from those of the present and SA models, especially on the upper wing surface.

IV.H. Free shear flow treatment

Obviously, the present model will not work for free shear flows where the wall distance y goes to infinity. In other words, there is no suitable length scale in regions away from walls and the entire model suffers from singularity. To avoid this situation, one can select $L \sim \delta$ where δ is the shear layer thickness. The following modifications are introduced to eradicate the wall-distance influence:

$$\begin{aligned} \epsilon &= A_\epsilon \frac{k^{3/2}}{L}, & A_\epsilon &= \max\left(0.25 + q_\epsilon; \frac{C_\mu^{3/4}}{\kappa}\right) \\ \frac{1}{L} &= \frac{C_\delta}{L_{vis}} = C_\delta\, C_\mu^* \sqrt{1 + \frac{\chi}{C_T}} \sqrt{\frac{\rho S}{\mu + \mu_T}}, & R_b &= \sqrt{C_\mu^*} \\ P_k &= \min\left[\left(\frac{P_k}{\epsilon}\right)\epsilon;\; k\, R_b\, S\right], & \mu_T &= \rho k T_t \min\left(C\mu; \frac{R_b}{\zeta}\right) \end{aligned} \tag{28}$$

where C_δ is a mixing-length matching parameter to be determined, depending on experimental data for free shear flows. It is anticipated that the characteristic of L_{vis} is analogous to that of the shear-layer thickness. The objective of this validation is to demonstrate that the proposed modifications comply with the computations of free shear flows (i.e., free jets). The SA and SST models contain the wall distance; they deserve modifications. Therefore, they will not be considered herein. Out of curiosity, the traditional ϵ-transport equation is included to make an assessment between one-equation (1Eq) and two-equation (2Eq) model computations. The ϵ-transport equation can be given as:

$$\frac{\partial \rho\epsilon}{\partial t} + \frac{\partial \rho u_j \epsilon}{\partial x_j} = \frac{\partial}{\partial x_j}\left[\left(\mu + \frac{\mu_T}{\sigma_\epsilon}\right)\frac{\partial k}{\partial x_j}\right] + \frac{\rho}{T_t}\left(C_{\epsilon 1}\, P_k - C_{\epsilon 2}\, \epsilon\right) \tag{29}$$

where $\sigma_\epsilon = 1.3$, $C_{\epsilon 1} = 1.44$ and $C_{\epsilon 2} = 1.8 - 1.9$. Calculations are performed for a plane jet with $Re \approx 3.4 \times 10^4$ and a round jet with $Re \approx 1.0 \times 10^5$. Figures 44 and 45 show the comparisons of the self-similar mean velocity profiles from the model predictions and the various measurements for the plane and round jets, respectively. The mean axial velocity u is normalized by the centre-line velocity u_c. In Fig. 46, the model predictions are compared with the measurements of Bradbury [47] and Heskestad [47] for the plane jet; $C_\delta = 2/3$ (for 1Eq model) and $C_{\epsilon 2} = 1.9$ (for 2Eq model) are used to match the experimental data. The 1Eq and 2Eq models provide likewise accurate predictions of the flow. Shown in Fig. 47 are the comparisons between the model predictions and the measurements of Rodi ,[49] and Wygnanski and Fiedler [50] for the round jet where $C_\delta = 0.5$ and $C_{\epsilon 2} = 1.81$ are prescribed to achieve good agreement with the data. Evidently, both models give similar accurate predictions of the flow with a smooth approach to the free-stream velocity.

The spreading rate is generally defined as the value of y/x where the velocity is half its center-line (maximum) value. The spreading rates given in Table 3 provide a concise criterion of the predictive capabilities of the turbulence models for free shear layers and confirm the quality of the turbulence models. The predicted spreading rates of both models fall within the range of measured values for the plane and round jets. To this end, it can be stressed that most popular turbulence models in the literature predict a stronger spreading of the round jet than that of the plane jet, which contradicts the measured data in Table 3; this phenomenon is known as the round/plane jet anomaly and is discussed at full length in .[51] However, this tendency of the turbulence models could be reduced by properly adjusting the model coefficients with experiments. To this end, it may be stressed that an average value of $C_\delta = (2/3 + 0.5) \approx 0.58$ can be used to compute both above-mentioned free shear flows.

V. Conclusions

The proposed turbulence model is sensitized to the near-wall and low-Reynolds number effects issuing from the physical requirements. The extended Bradshaw-relation R_b (i.e., empirical coefficient of production P_k) and dissipation terms render the model to account for non-local and geometry effects. The anisotropic production in the k–equation is accounted for substantially by modifying the production–to–dissipation ratio $P_k/\epsilon = \min\left[f_\mu\left(\frac{P_k}{\epsilon}\right); R_b\, S\, T_t\right]$, leading to a reduced level of turbulence generation in non-equilibrium flow regions. Thus the resulting production term P_k is capable of capturing some features of stress-strain misalignment on the evolution of turbulence levels in a linear eddy-viscosity model. Consequently, the model extends the ability of one-equation models to account for non-equilibrium and anisotropic effects. In addition, the non-linear function q_ϵ augments the dissipation-rate in the vicinity of the wall and the eddy-viscosity formulation has a close resemblance to the Menter SST k–ω model. Comparing the predicted results with measurements for the flow cases considered, demonstrates that the present model offers some improvement over the SA model and stays competitive with the SST k–ω model.

In particular, most researchers have given up the k-equation model in the favor of one-equation models based on the transport equations for the eddy-viscosity. Nevertheless, the current study presents an open framework for turbulence modeling, in which the algebraically determined anisotropic formulation for dissipation-rate calls for more innovative ideas. This aspect enables the model to handle the adverse pressure-gradient flows with induced separation and reattachment very well. Computational experience approves that the present model does not need a finer grid near the wall as required by a zero-equation algebraic model; it is robust and a quick convergence can be expected. The performance evaluation dictates that the proposed model may be a good choice for engineering applications, since it can easily be extended to a non-linear eddy viscosity model, scale-adaptive simulation (SAS; incorporating the model dependency on the von Karman length scale) and detached eddy simulation (DES) modes. The current turbulence model is promising, however, additional validations are necessary to gain confidence in the proposed approach.

VI. Acknowledgents

We are grateful to the National Natural Science Foundation of China (No. 51709070), Natural Science Foundation of Zhejiang Province (LQ17E090007), Key R& D Program of Zhejiang Province (2018C04002).

References

[1]Norris LG, Reynolds WC: Turbulent channel flow with moving wavy boundary. *Report No. FM–10*, Stanford University, Department of Mechanical Engineering, USA, 1975.

[2]Rahman MM, Lampinen MJ, Siikonen T: An improved k–equation turbulence Model. *Journal of Energy and Power Engineering*, 8:1895-1907;2014.

[3]Rahman MM, Agarwal RK, Siikonen T: A modified one-equation turbulence model based on turbulent kinetic energy equation. *54th AIAA Aerospace Sciences Meeting*, pp.1598;2016.

[4]Xu J, Zhang Y, Bai J: One-equation turbulence model based on extended Bradshaw assumption. *AIAA Journal*, 53(6):735-747;2015.

[5]Wilcox DC: Turbulence modeling for CFD. 2nd ed. DCW Industries, 1998.

[6]Baldwin BS, Barth TJ: A one-equation turbulence transport model for high-Reynolds number wall-bounded flows. *NASA TM-102847*, 1990.

[7]Spalart PR, Allmaras SR: A one-equation turbulence model for aerodynamic flows. *AIAA Paper No. 92-0439*, 1992.

[8]Menter FR: Eddy viscosity transport equations and their relation to the k–ϵ model. *ASME Journal of Fluids Engineering*, 119:876-884;1997.

[9]Elkhoury M: Assessment and modification of one-equation models of turbulence for wall-bounded flows. *ASME Journal of Fluids Engineering*, 129:921-928;2007.

[10]Fares E, Schröder W: A general one-equation turbulence model for free shear and wall-bounded flows. *Flow, turbulence and combustion*, 73:187-215;2000.

[11]Nagano Y, Pei CQ, Hattori H: A new low-Reynolds-number one-equation model of turbulence. *Flow, turbulence and combustion*, 63:135-151;1999.

[12]Rahman MM, Siikonen T, Agarwal RK: Improved low Re–number one–equation turbulence model. *AIAA Journal*, 49:735-747:2011.

[13]Rahman MM, Wallin S, Siikonen T: Exploring k and ϵ with R–equation model using elliptic relaxation function. *Flow, Turbulence and Combustion*, 89:121-148;2012.

[14]Rahman MM, Agarwal RK, Siikonen T: RAS one-equation turbulence model with non-singular eddy-viscosity coefficient. *International Journal of Computational Fluid Dynamics*, 30(2):89-106;2016.

[15]Bradshaw P, Ferriss DH, Atwell NP: Calculation of boundary layer development using the turbulent energy equations. *Journal of Fluid Mechanics*, 23:31–64;1967.

[16]Menter FR: Two-equation eddy-viscosity turbulence models for engineering applications. *AIAA Journal*, 32(8):1598-1605;1994.

[17]Rodi W: A new algebraic relation for calculating the Reynolds stresses. *Z. Angew. Math. Mech.*, 56, T219-221;1976.

[18]Abid R, Morrison JH, Gatski TB, Speziale CG: Prediction of aerodynamic flows with a new explicit algebraic stress model. *AIAA Journal*, 34:2632-2635;1997.

[19]Gatski TB, Speziale CG: On the explicit algebraic stress models for complex turbulent models. *Journal of Fluid Mechanics*, 254:59-78;1993.

[20]Speziale CG, Sarkar S, Gatski TB: Modelling the pressure-stain correlation of turbulence: An invariant dynamical system. *Journal of Fluid Mechanics* 227:245-272;1991.

[21]Girimaji SS. Fully explicit and self-consistent algebraic Reynolds stress model. *Theoretical and Computational Fluid Dynamics* 8:387-402;1996.

[22]Jogen J, Gatski TB: A new approach to characterizing the equilibrium states of the Reynolds stress anisotropy in homogeneous turbulence. *Theoretical and Computational Fluid Dynamics*, 11:31-47;1998.

[23]Rahman MM, Siikonen T: An eddy viscosity model with near-wall modifications. *International Journal of Numerical Methods in Fluids*, 49:975-997;2005.

[24]Rahman MM, Siikonen T: Modifications for an explicit algebraic stress model. *International Journal of Numerical Methods in Fluids*, 35(2):221–245;2001.

[25]Andreas EL, Claffery KJ, Jordan RE, Fairall CW, Guest PS, Persson POG, Grachev AA: Evaluations of the von Karman constant in the atmospheric surface layer. *Journal of Fluid Mechanics*, 559;117–149:2006.

[26]She ZS, Chen X, Wu Y, Hussain F: New perspective in statistical modeling of wall–bounded turbulence. *Acta Mechanica Sinica*, 26(6):847–861;2010.

[27]Mansour NN, Kim J, Moin P: Reynolds-stress and dissipation-rate budgets in a turbulent channel flow. *Journal of Fluid Mechanics* 194:15-44;1988.

[28]Revell AJ, Craft TJ, Laurence DR: Turbulence modelling of unsteady turbulent flows using the stress strain lag model. *Flow, Turbulence and Combustion*, 86;129–151:2011.

[29]Kim J, Moin P, Moser R. Turbulence statistics in fully developed channel flow at low Reynolds number. *Journal of Fluid Mechanics* 177:133-166;1987

[30]Lee MJ, Kim J, Moin P. Structure of turbulence at high shear rate. *Journal of Fluid Mechanics* 216:561-583;1990

[31]Rogers MM, Moin P. The structure of the vorticity field in homogeneous turbulent flows. *Journal of Fluid Mechanics* 176:33-66;1987

[32]Kim J: "Personal communication". 1990.

[33]Tavoularis S, Corrsin A: Experiments in nearly homogeneous turbulent shear flow with a uniform mean temperature gradient. Part I, *Journal of Fluid Mechanics*, 104:311-347;1981.

[34]Rahman MM, Rautaheimo P, Siikonen T: Numerical study of turbulent heat transfer from a confined impinging jet using a pseudo-compressibility method. *In Second International Symposium on Turbulence, Heat and Mass transfer*, Delft, The Netherlands, K. Hanjalic K, Peeters TWJ (eds). Delft University Press: Delft, 511-520;1997.

[35]Rahman MM, Siikonen T: An artificial compressibility method for incompressible flows. *Numerical Heat Transfer, Part B*, 40:391-409;2001.

[36]Rahman MM, Siikonen T: An artificial compressibility method for viscous incompressible and low Mach number flows. *International Journal for Numerical Methods in Engineering*, 75:1320-1340;2008.

[37]Roe PL: Approximate Riemann solvers, parameter vectors, and difference schemes. *Journal of Computational Physics*, 43(2):357-372;1981.

[38]Lombard C, Bardina J, Venkatapathy E, J. Oliger J: Multi–dimensional formulation of CSCM - an upwind flux difference eigenvector split method for the compressible Navier–Stokes equations. *In 6th AIAA Computational Fluid Dynamics Conference* , AIAA Paper 83-1895-CP, 649-664;1983.

[39]Jameson A, Yoon S: Multigrid solution of the Euler equations using implicit schemes. *AIAA Journal*, 24(11):1737-1743;1986.

[40]Driver DM, Seegmiller HL: Features of a reattaching turbulent shear layer in divergent channel flow. *AIAA Journal*, 23(2):163-171;1985.

[41]So RMC, Lai YG, Yoo GJ: Low-Reynolds number modeling of flows over a backward facing step. *J. Appl. Math. Phys.*, 39:13-27;1988.

[42]Buice C, Eaton JK: Experimental investigation of flow through an asymmetric plane diffuser. *Dept. of Mechanical Engineering, Thermoscience Div.*, Rept. TSD-107, Stanford University, California, CA,1997.

[43]Simpson RL, Long CH, Byun G: Study of vortical separation from an axisymmetric hill. *Int. J. Heat Fluid Flow*, 23:582-591;2002.

[44]Coles D, Wadcock AJ: Flying-hot-wire study of flow past an NACA 4412 airfoil at maximum lift. *AIAA Journal*, 17(4):321-329;1979.

[45]Turbulence Modeling Resource [online database] NASA Langley Research Center, Hampton, VA, http://turbmodels.larc.nasa.gov/.

[46]Schmitt V, Charpin F: Pressure distributions on the ONERA M6–Wing at Transonic Mach Number. *in AGARD–AR–138*, B1–1–B1–44, May 1979.

[47]Bradbury JS: The structure of a self-preserving turbulent plane jet. *J. Fluid Mech.*, 23(1):31-64;1965.

[48]Heskestad G: Hot-wire measurements in a plane turbulent jet. *J. Appl. Mech.*, 32(4):721-734;1965.

[49]Rodi W: A new method for analyzing hot-wire signals in highly turbulent flows and its evaluation on round jets. *Disa Information*, 17:9-18;1975.

[50]Wygnansk I, Fiedler HE: Some measurements in self-preserving jet. *J. Fluid Mech.*, 38(3):577-612;1969.

[51]Pope SB: An explanation of the turbulent round-jet/plane-jet anomaly. *AIAA J.*, 16(3):279-281;1978.

Table 1. Anisotropy in the log layer of channel flow

b_{ij}	DNS	$Standard$	$Present$
b_{12}	-0.145	-0.149	-0.147

Table 2. Anisotropy in the homogeneous shear flow

b_{ij}	$Experiment$	$Standard$	Present
b_{12}	-0.142	-0.273	-0.150

Table 3. Spreading rates for turbulent free shear flows

Flow	1Eq model	2Eq model	Measured
Plane jet	0.106	0.106	$0.1 - 0.11$
Round jet	0.0931	0.0924	$0.086 - 0.096$

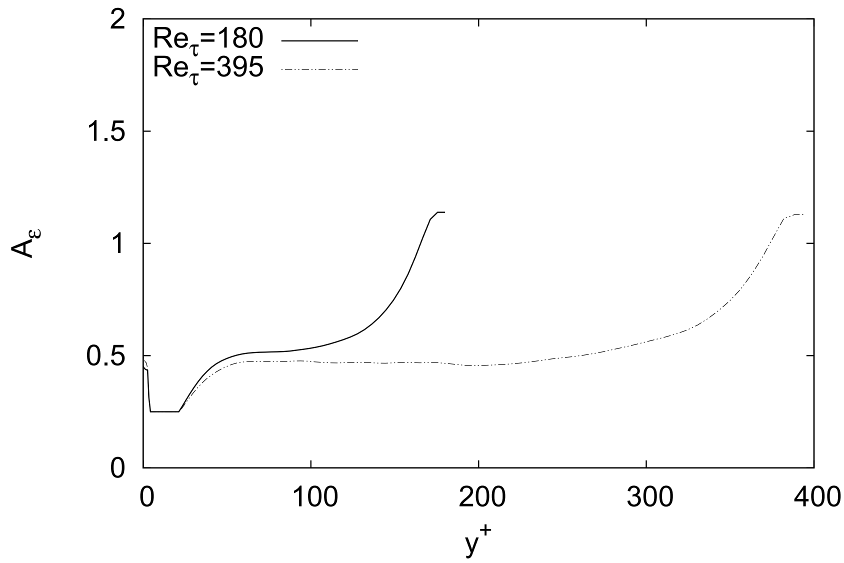

Figure 1. Variations of dissipation coefficient A_ϵ with wall distance in channel flow.

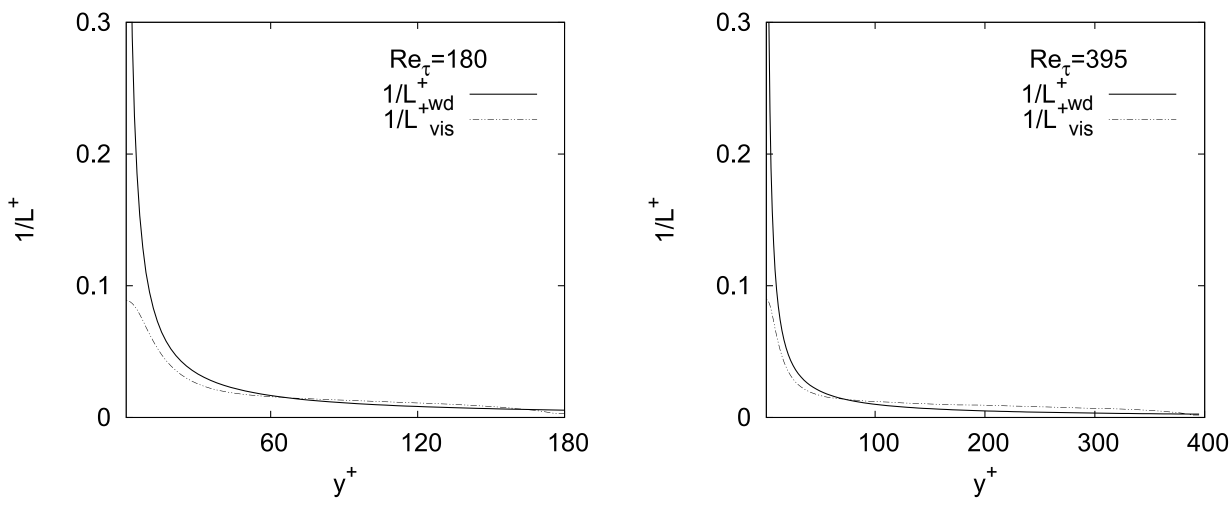

Figure 2. Variations of inverse length scales with wall distance in channel flow.

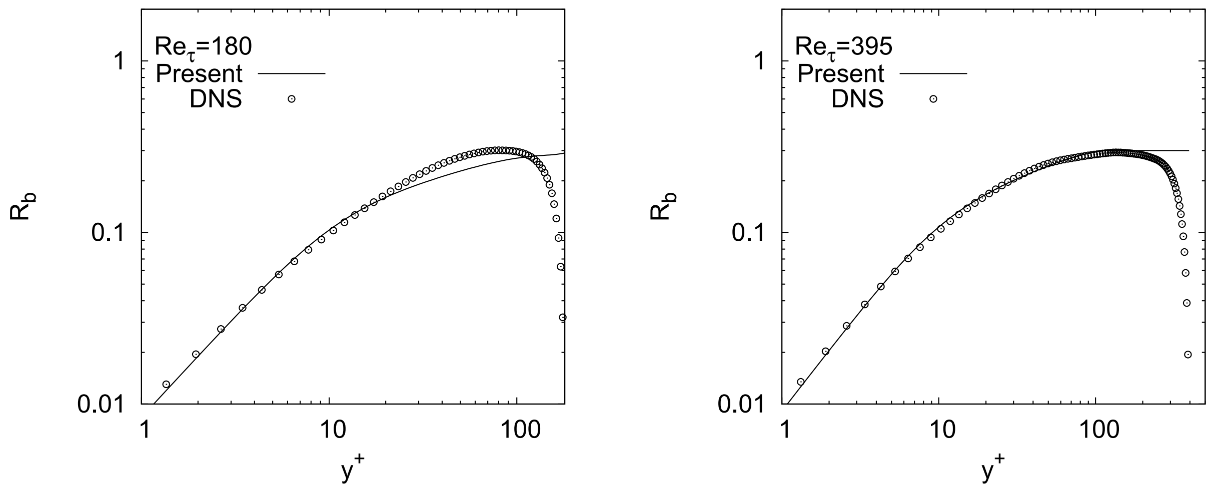

Figure 3. Near–wall behavior of stress-intensity parameter R_b.

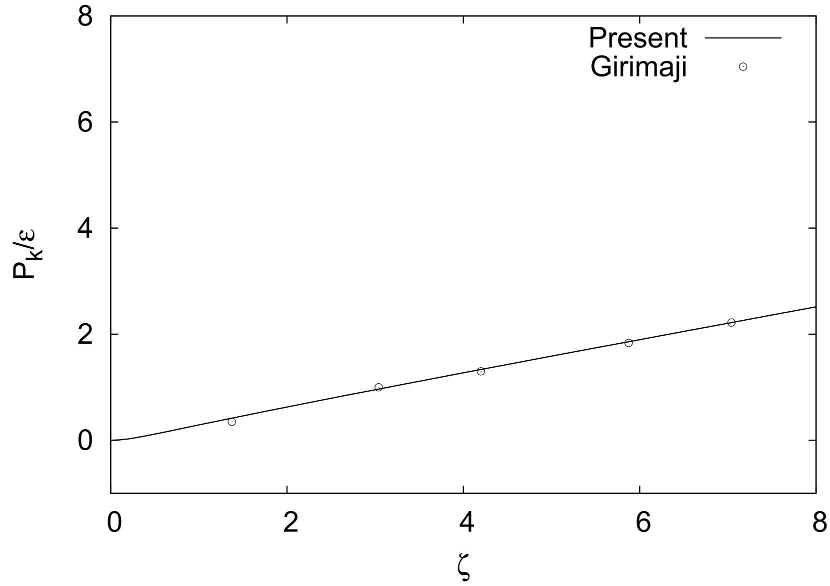

Figure 4. Locus of solution points for state variable P_k/ϵ as a function of ζ ($\Re = 1$).

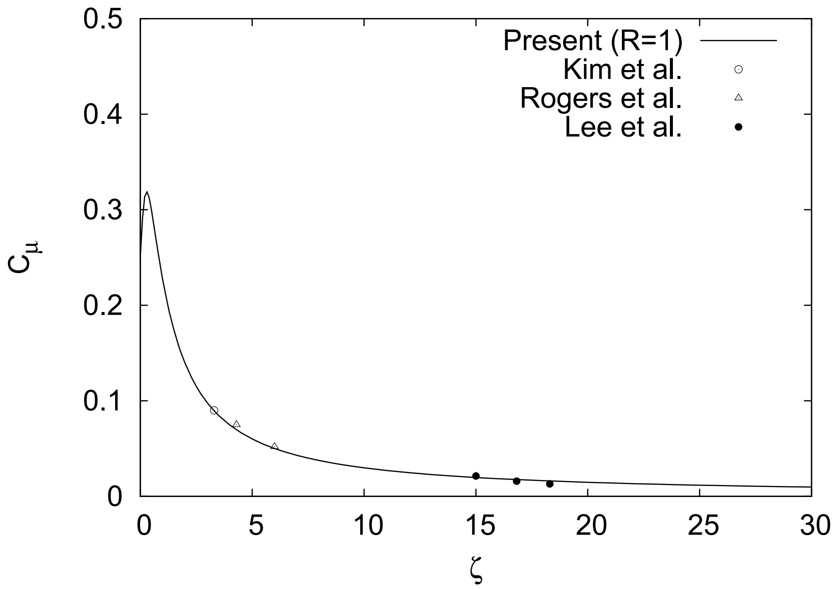

Figure 5. Distribution of C_μ as a function of shear/strain-rate parameter ζ.

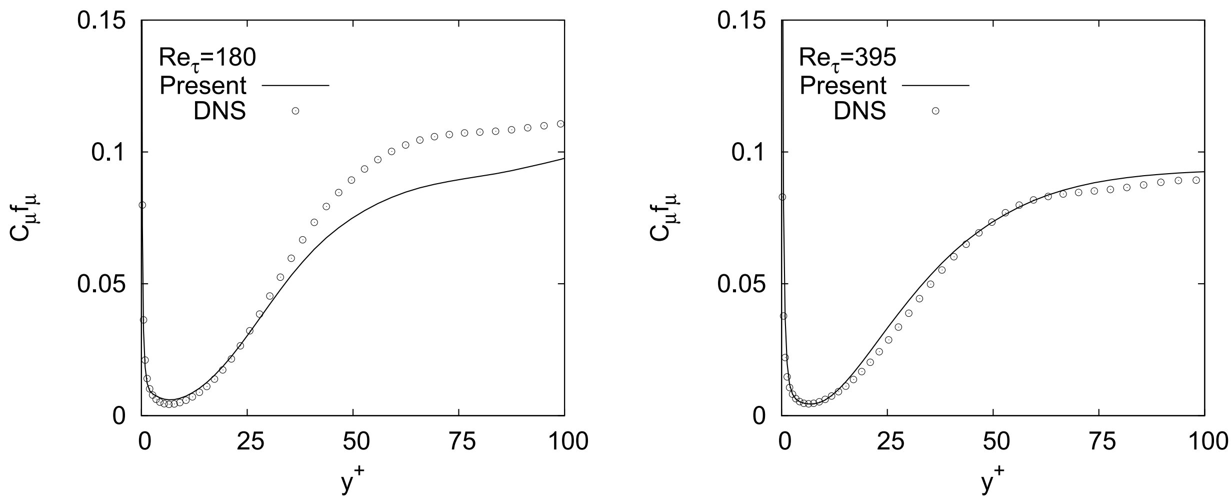

Figure 6. Variations of eddy–viscosity coefficients with wall distance in channel flow.

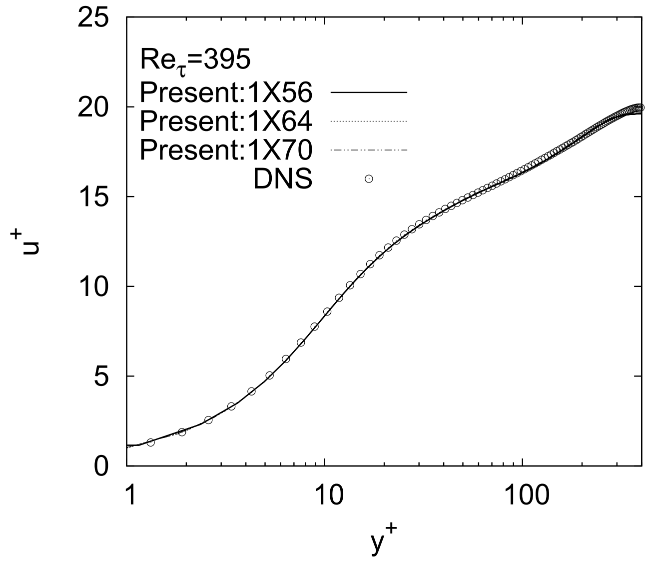

Figure 7. Effect of grid density on mean velocity profile in turbulent channel flow at $Re_\tau = 395$ with present model.

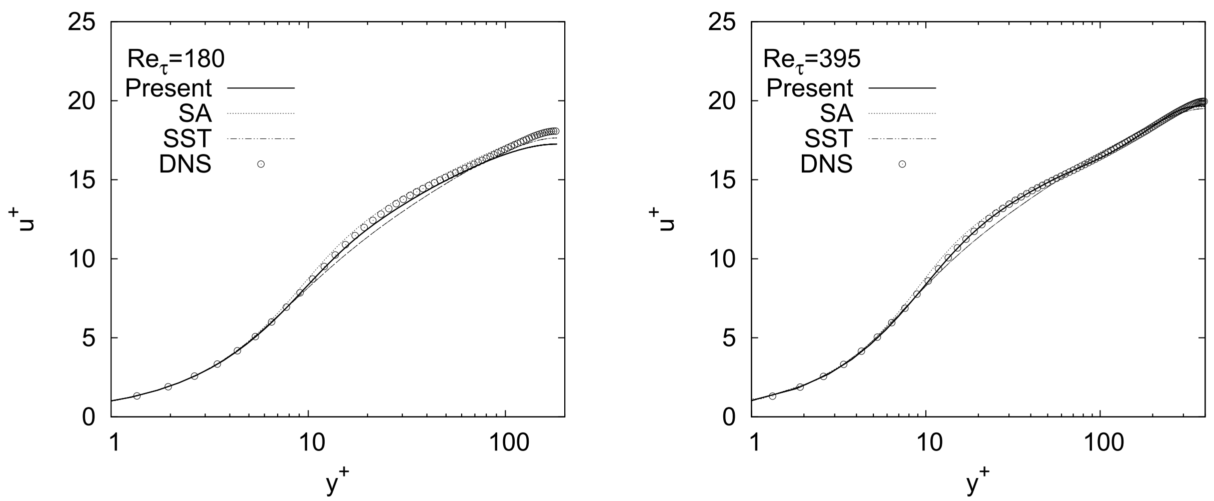

Figure 8. Mean velocity profiles of channel flow.

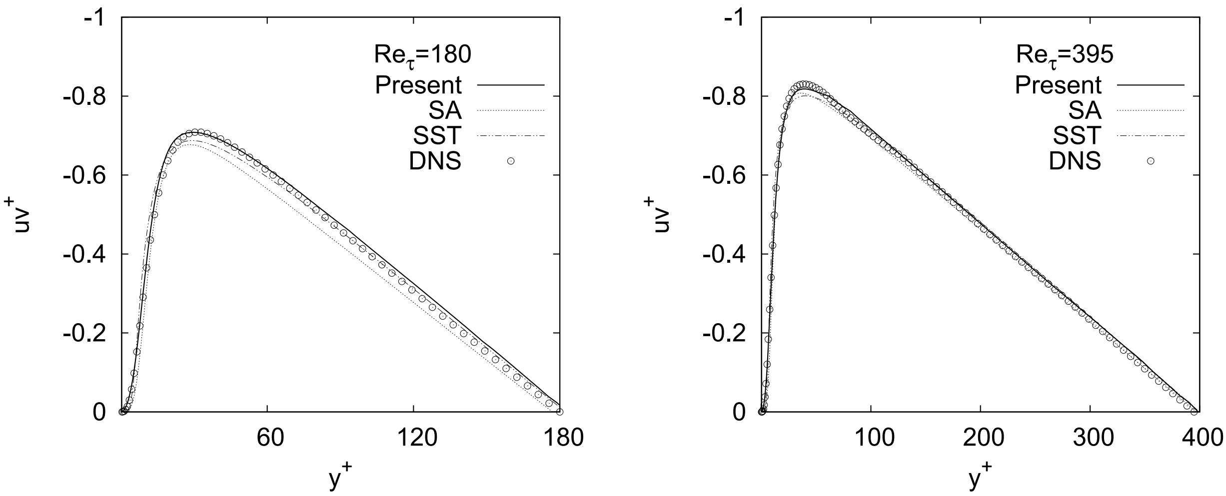

Figure 9. Shear stress profiles of channel flow.

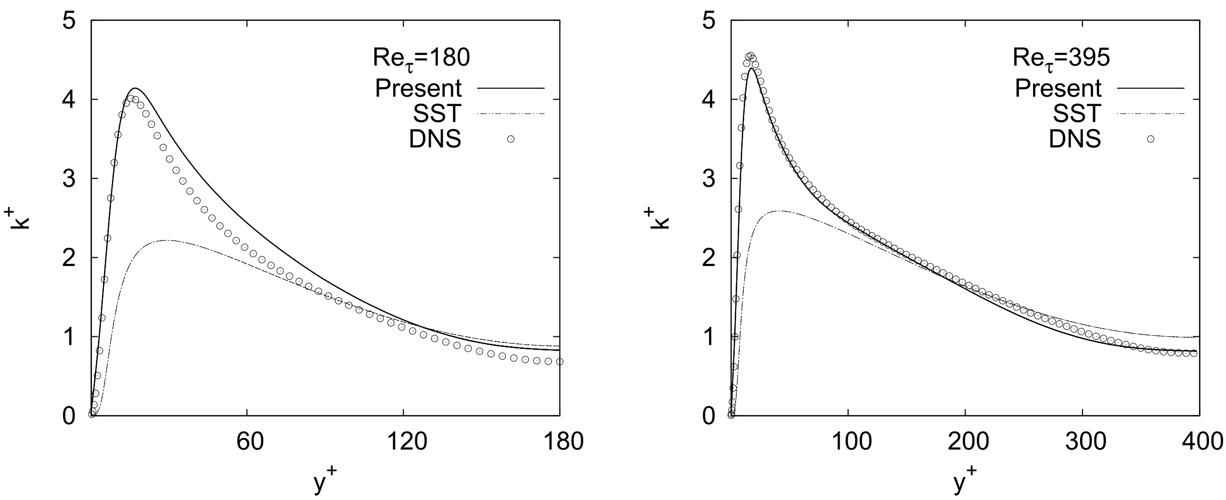

Figure 10. Turbulence kinetic energy profiles of channel flow.

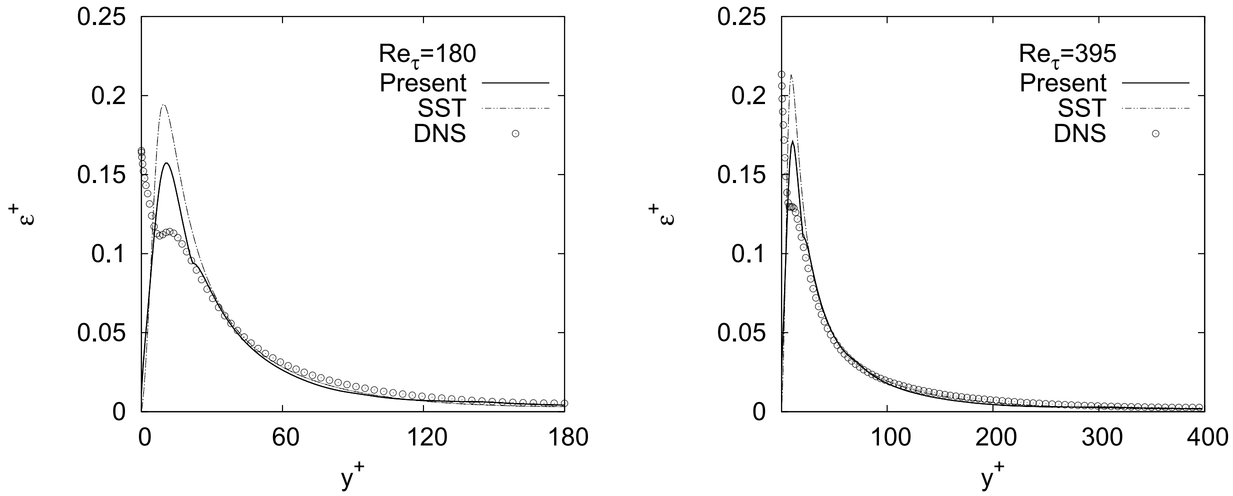

Figure 11. Dissipation rate profiles of channel flow.

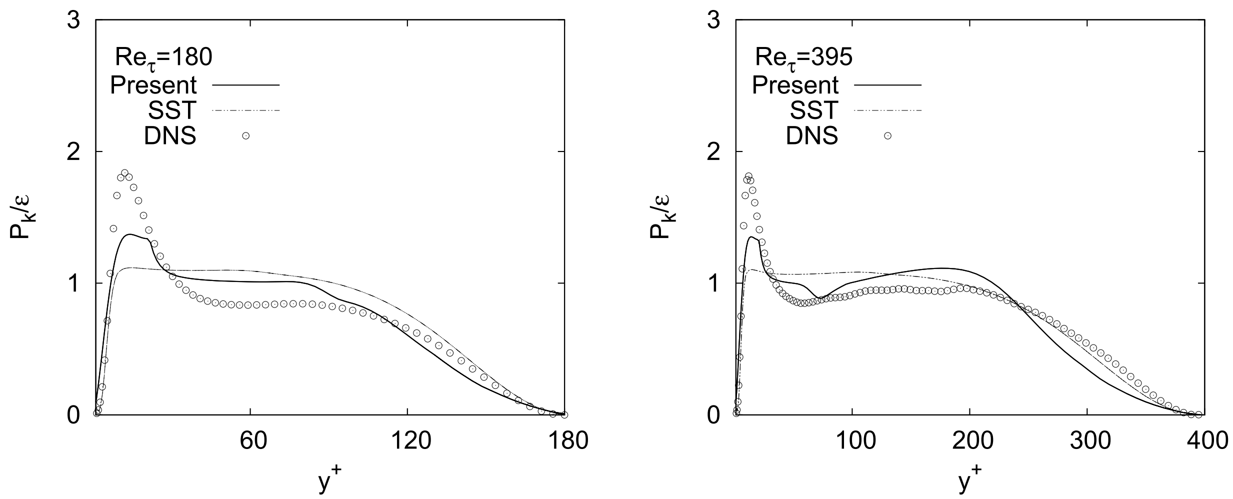

Figure 12. P_k/ϵ **profiles of channel flow.**

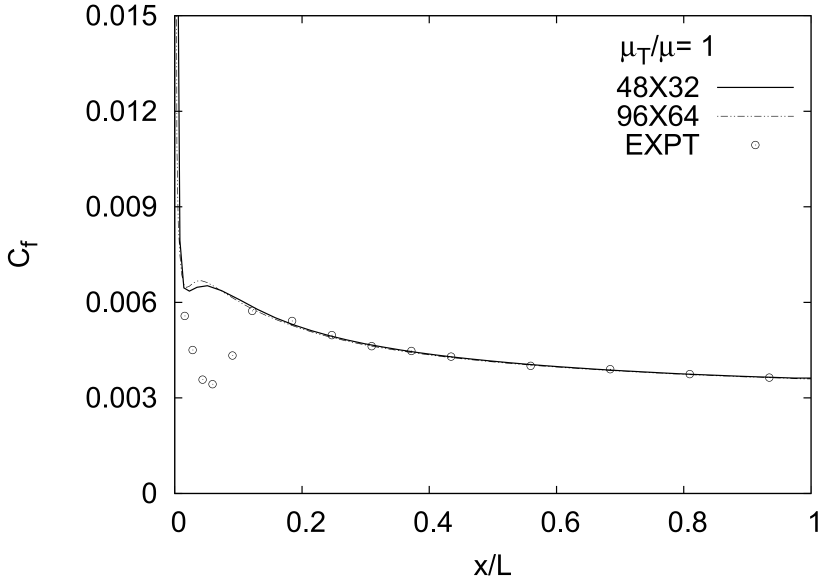

Figure 13. Grid convergence study of present model with $\mu_T/\mu = 1$ in skin-friction profile for flat-plate case.

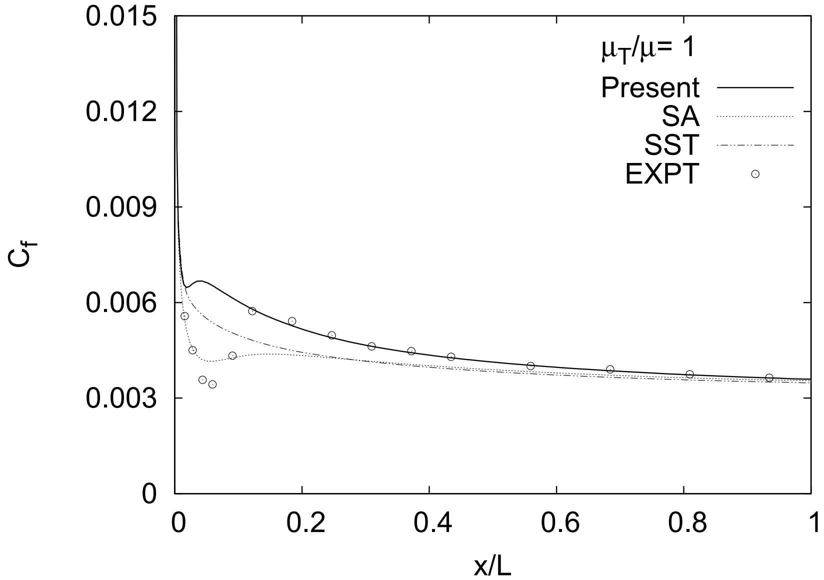

Figure 14. Skin-friction profiles for flat-plate case with $\mu_T/\mu = 1$.

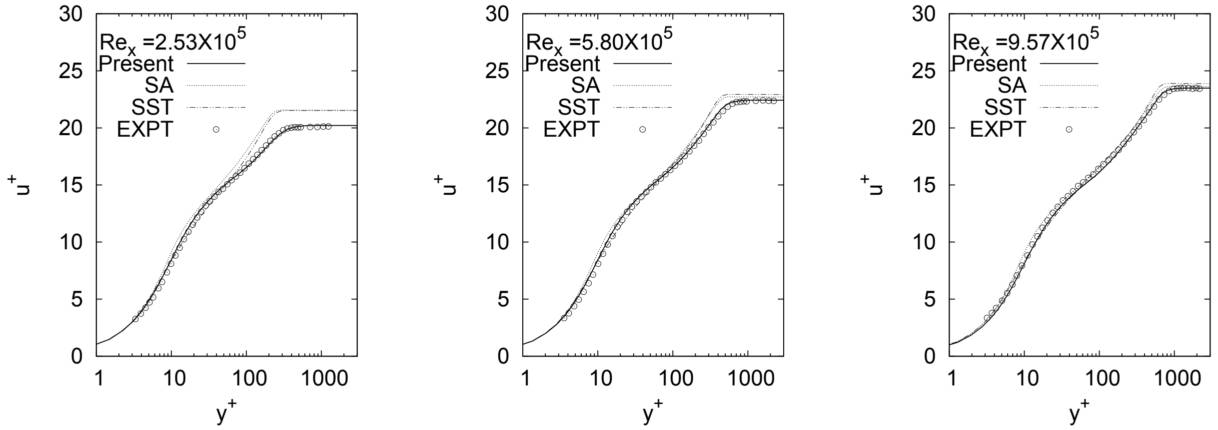

Figure 15. Mean velocity profiles for flat-plate case at different down-stream stations: $x = (0.395, 0.895, 1.495)\ m$.

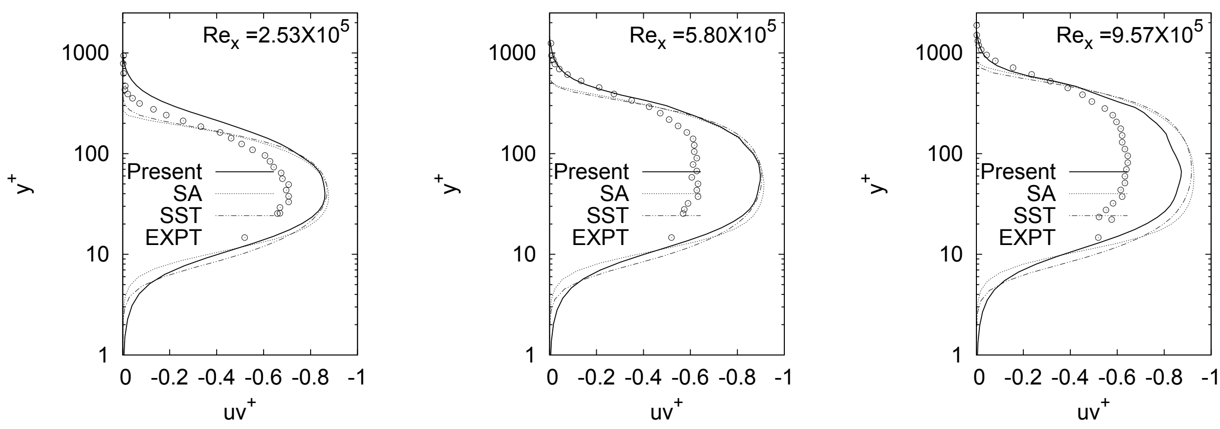

Figure 16. Shear stress profiles for flat-plate case at different down-stream stations: $x = (0.395, 0.895, 1.495)\ m$.

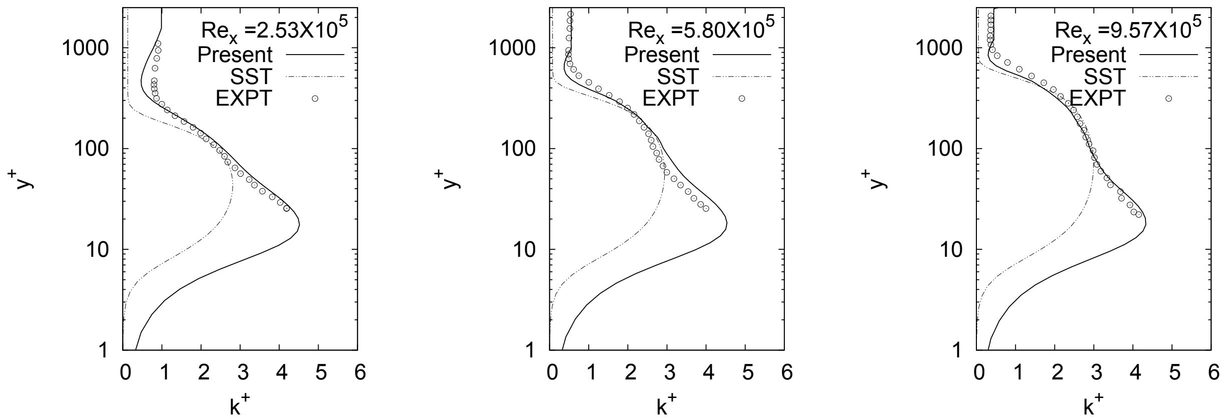

Figure 17. Kinetic energy profiles for flat-plate case at different down-stream stations: $x = (0.395, 0.895, 1.495)\ m$**.**

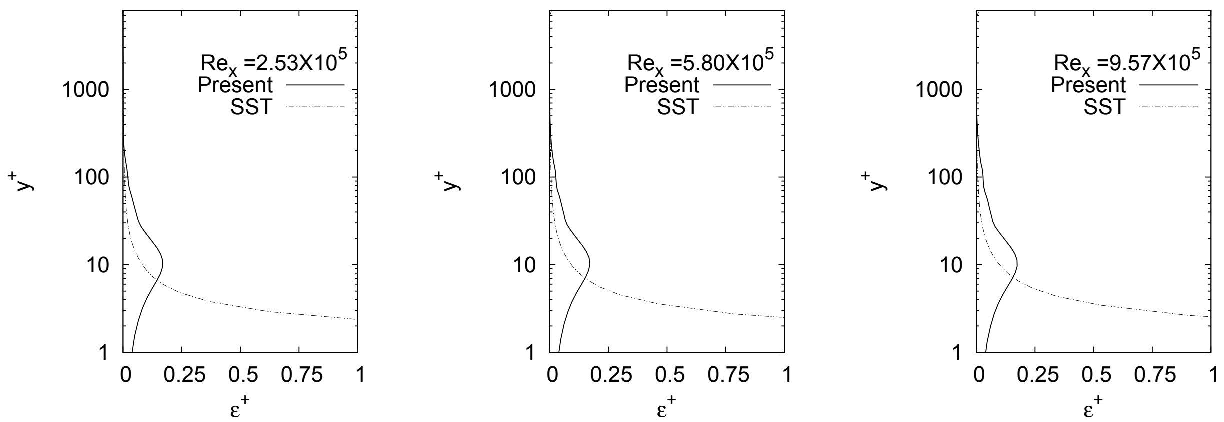

Figure 18. Dissipation-rate profiles for flat-plate case at different down-stream stations: $x = (0.395, 0.895, 1.495)\ m$**.**

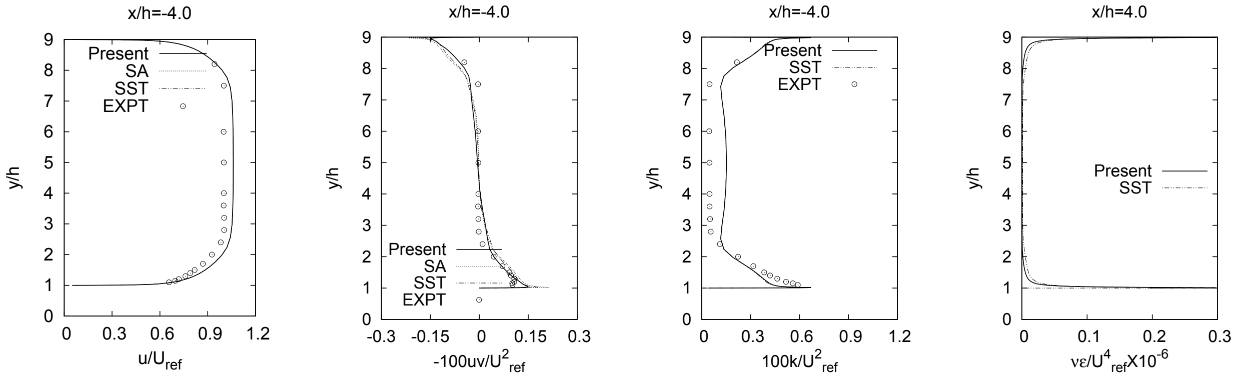

Figure 19. Inlet profiles for step flow.

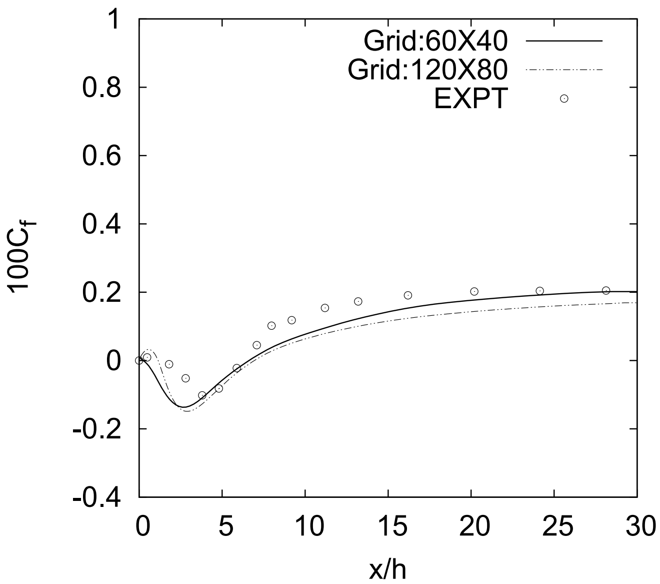

Figure 20. Grid convergence study of present model in skin-friction profile for step flow.

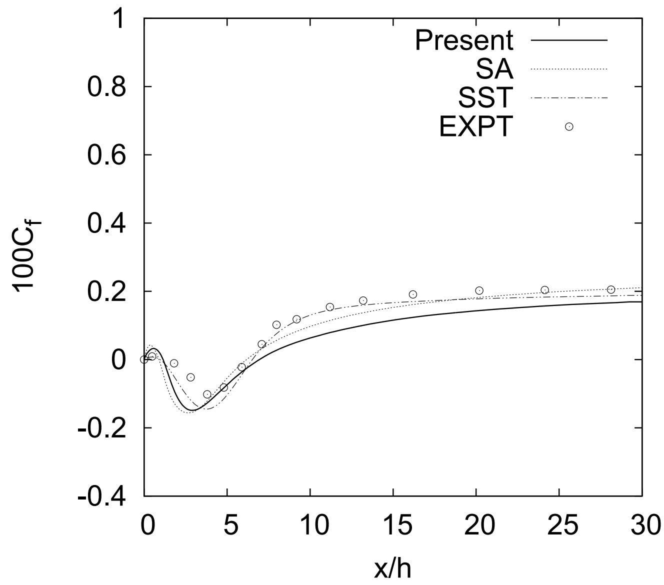

Figure 21. Skin-friction profiles for step flow case along bottom wall.

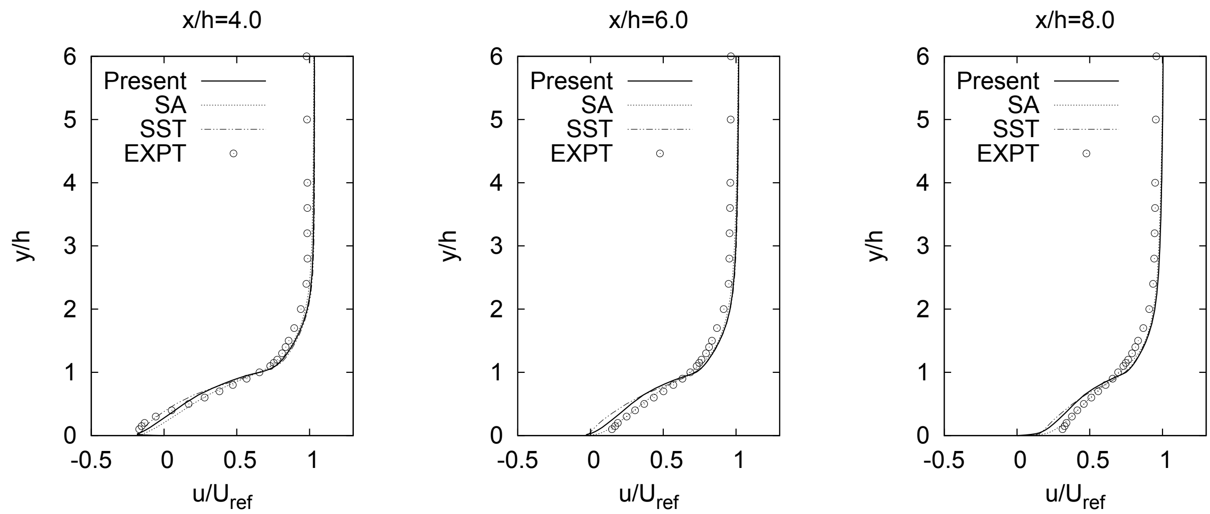

Figure 22. Mean velocity profiles at selected locations for step flow.

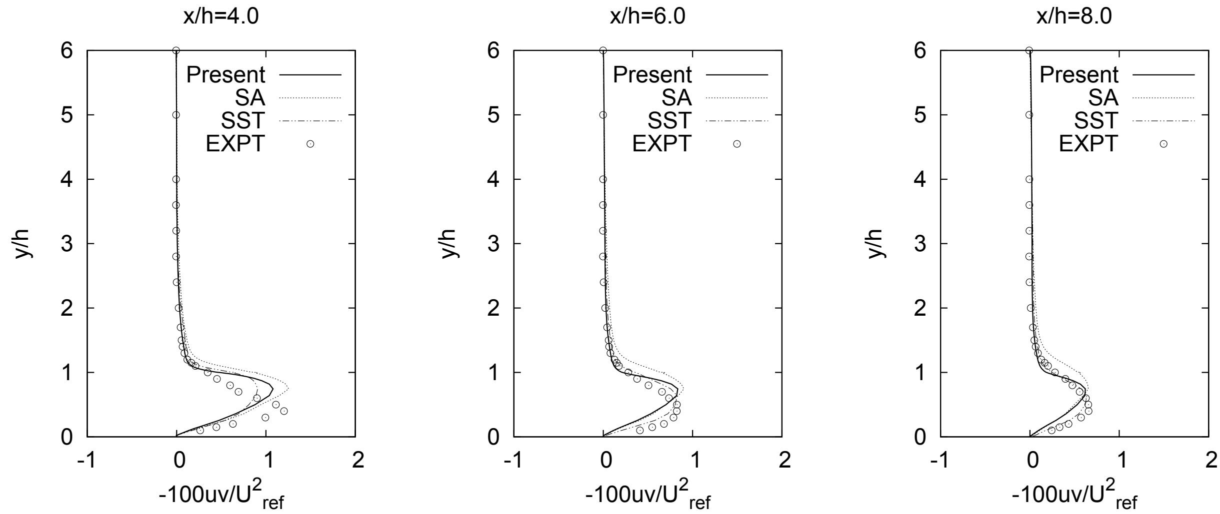

Figure 23. Shear stress profiles at selected locations for step flow.

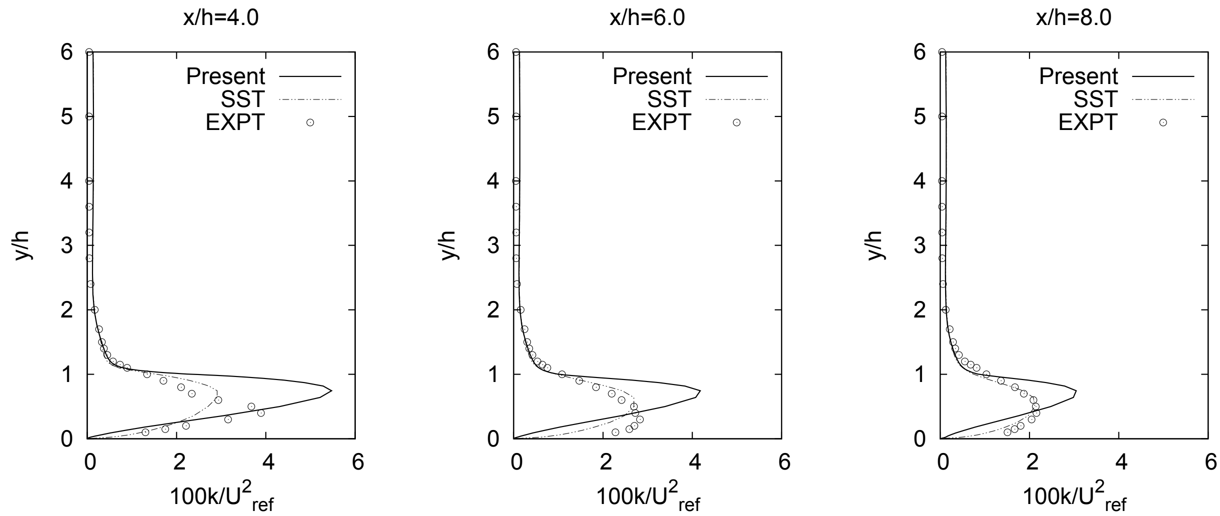

Figure 24. Kinetic energy profiles at selected locations for step flow.

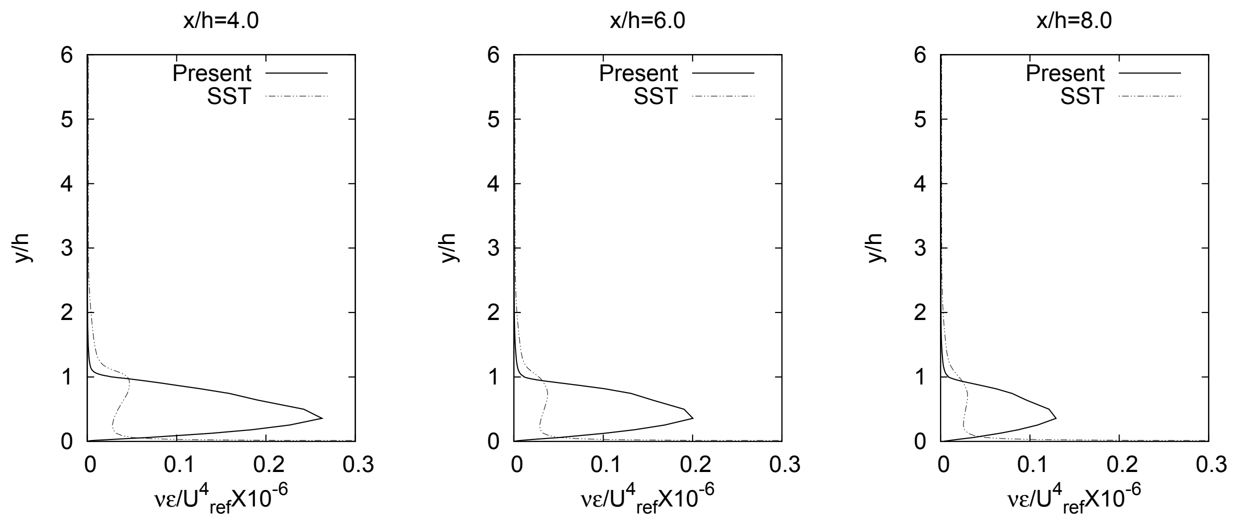

Figure 25. Dissipation-rate profiles at selected locations for step flow.

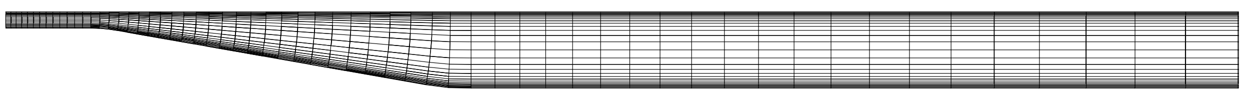

Figure 26. Computational grid for diffuser flow.

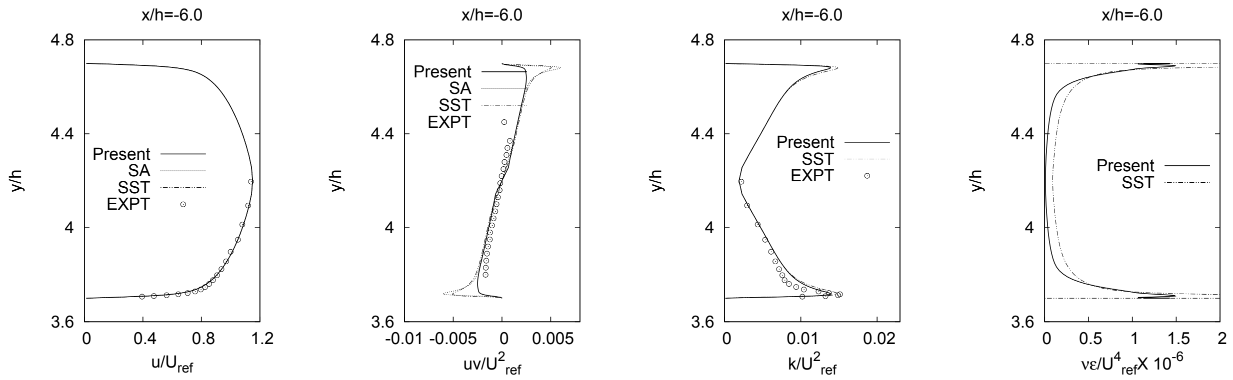

Figure 27. Inlet velocity, shear stress, kinetic energy and dissipation-rate profiles for diffuser flow.

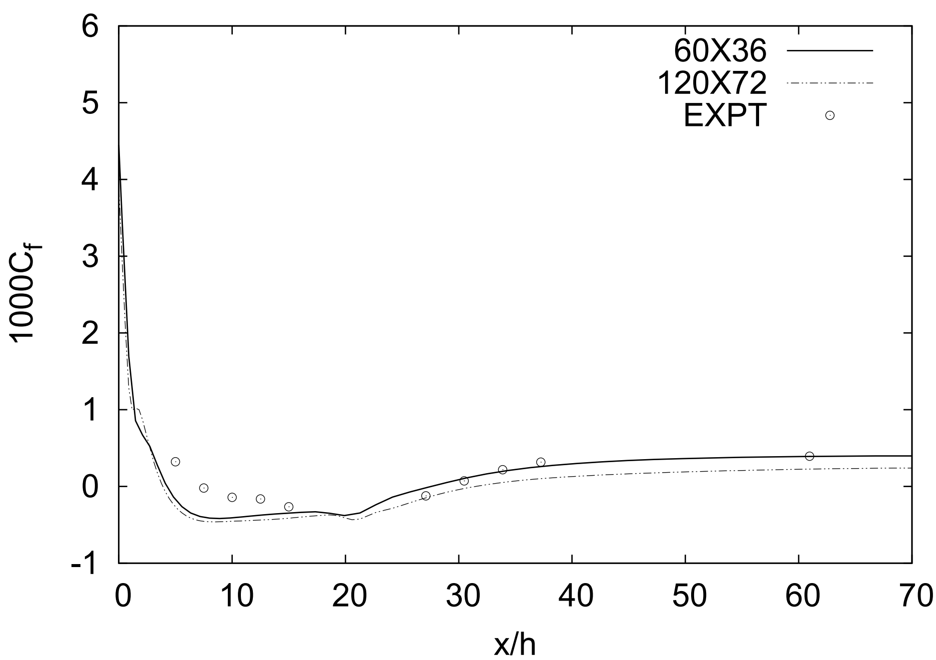

Figure 28. Effect of grid density on skin-friction coefficient of turbulent diffuser flow along deflected bottom wall with present model.

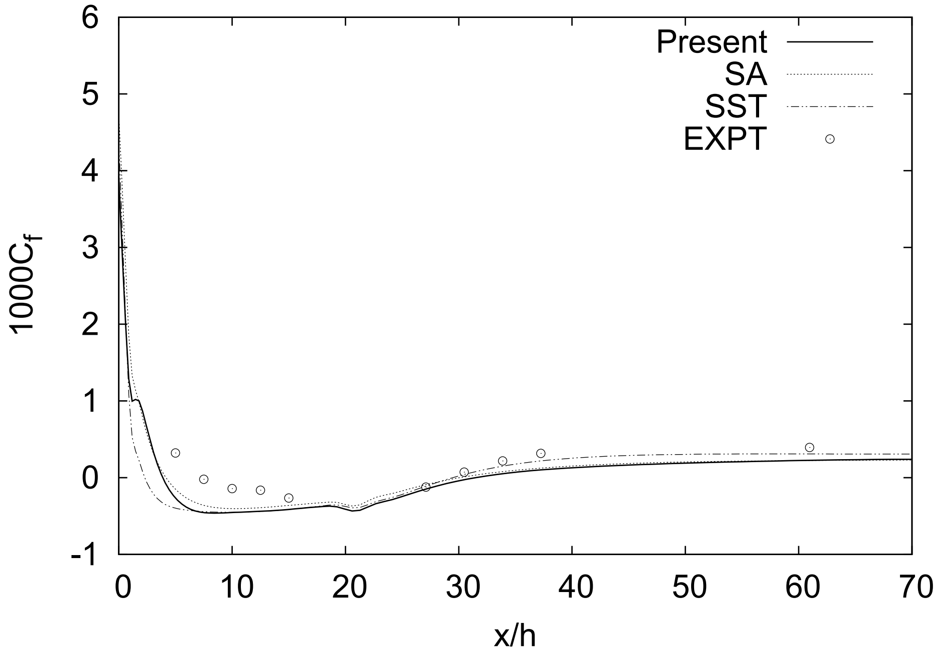

Figure 29. Skin-friction coefficient along deflected bottom wall of diffuser flow.

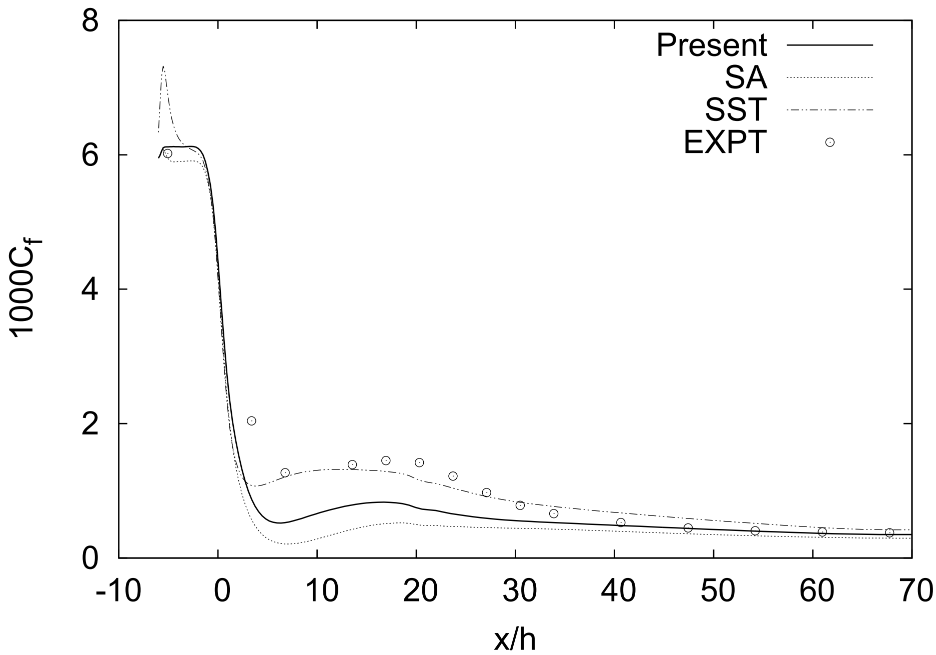

Figure 30. Skin-friction coefficient along straight top wall of diffuser flow.

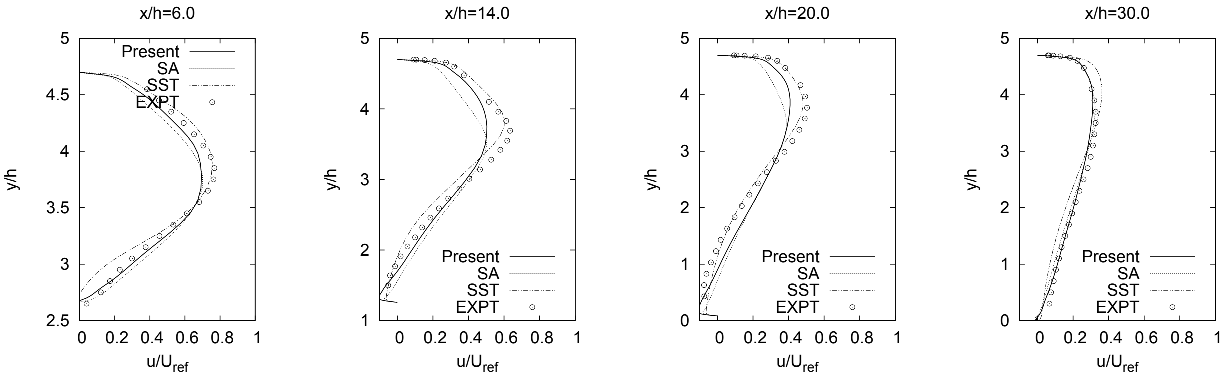

Figure 31. Mean velocity profiles at selected locations for diffuser flow.

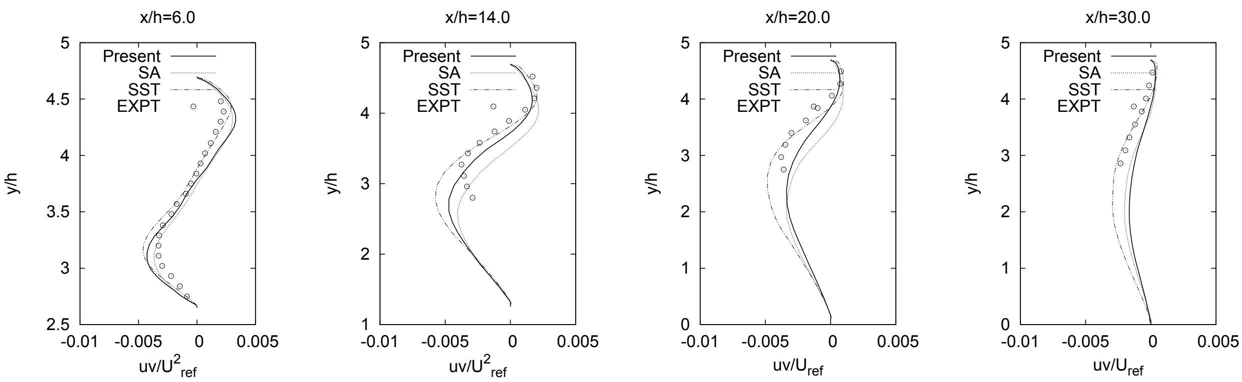

Figure 32. Shear stress profiles at selected locations for diffuser flow.

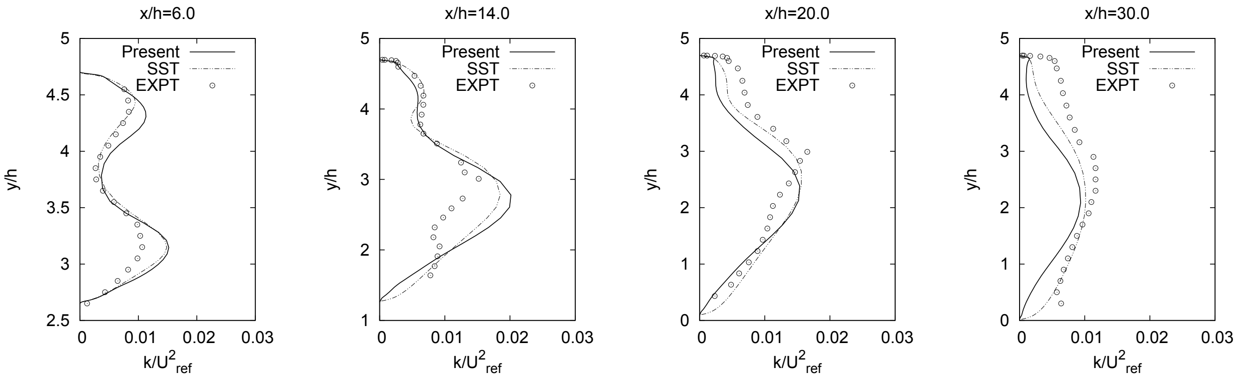

Figure 33. Kinetic energy profiles at selected locations for diffuser flow.

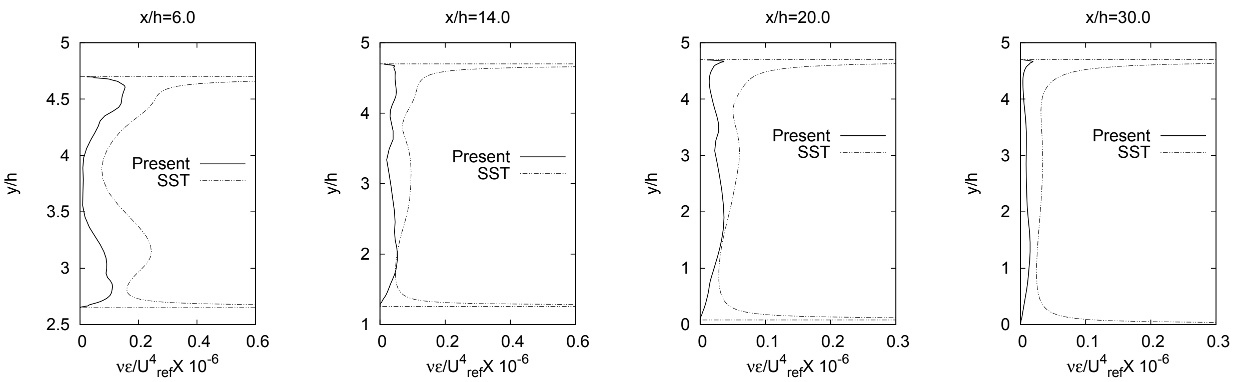

Figure 34. Dissipation-rate profiles at selected locations for diffuser flow.

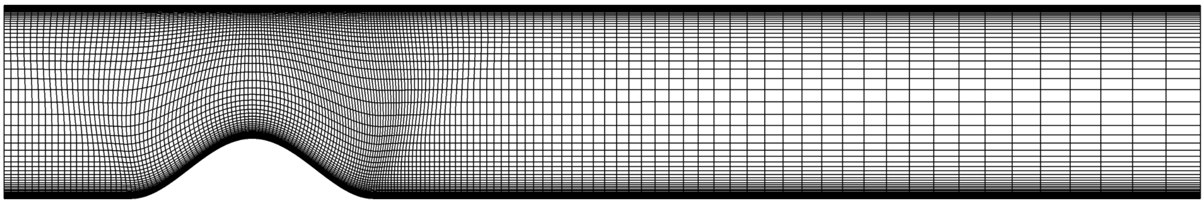

Figure 35. Computational grid in symmetry plane $z/h = 0$ for 3D hill flow.

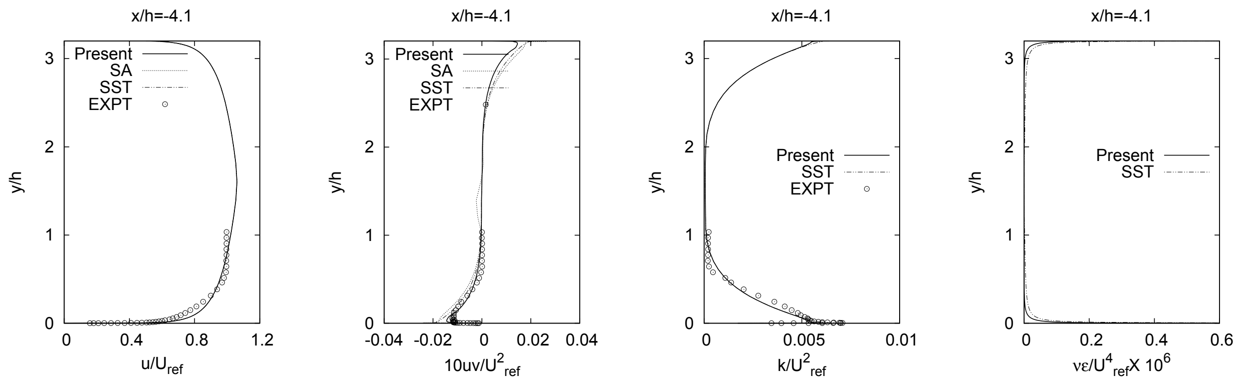

Figure 36. Inlet velocity, shear stress, kinetic energy and dissipation-rate profiles for 3D hill flow flow.

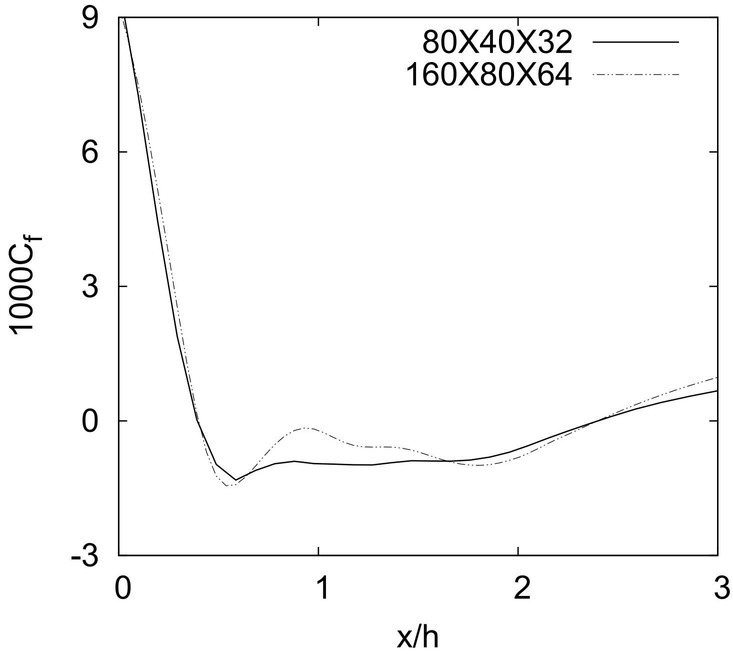

Figure 37. Effect of grid density on skin-friction coefficient along 3D hill surface in the center-plane $z/h = 0$ with present model.

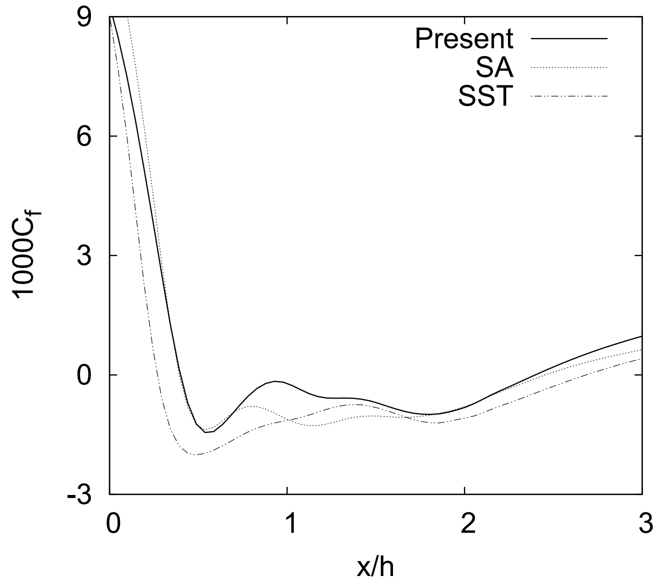

Figure 38. Skin-friction coefficients along 3D hill surface in the center-plane $z/h = 0$.

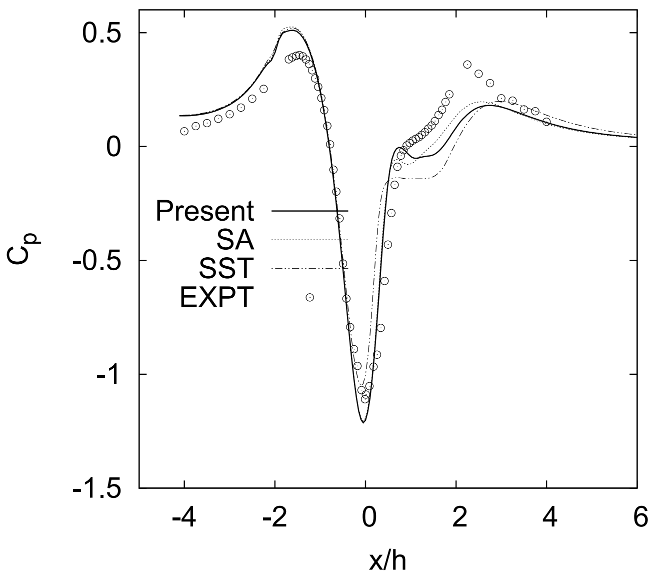

Figure 39. Pressure coefficients along 3D hill surface in the center-plane $z/h = 0$.

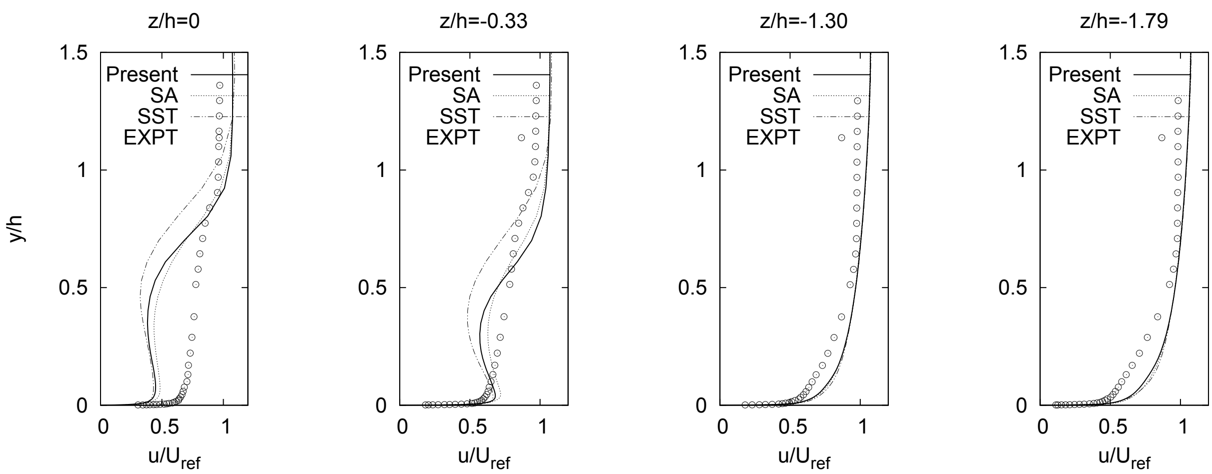

Figure 40. Streamwise velocity profiles at selected spanwise locations in the downstream plane at $x/h = 3.69$ for 3D hill flow..

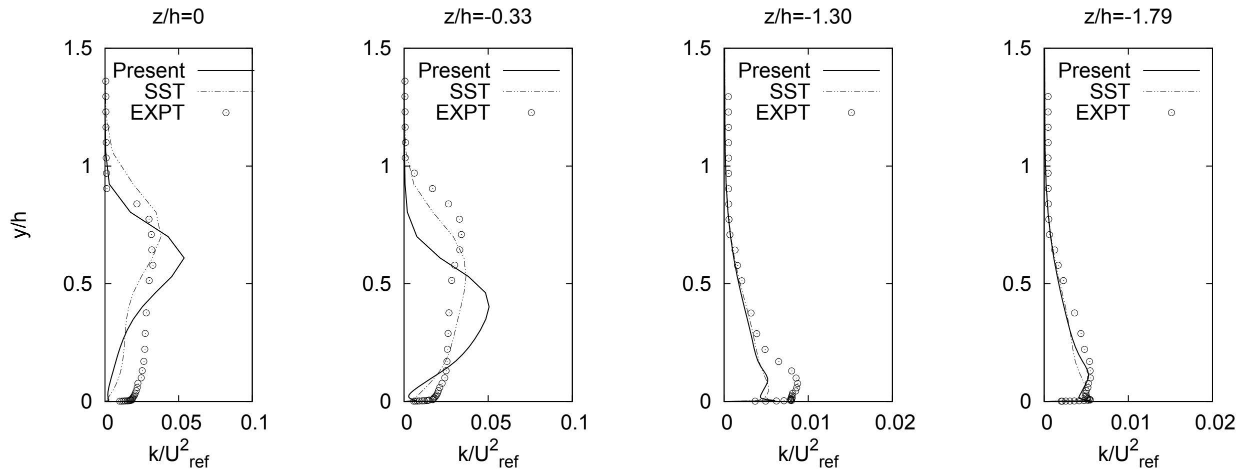

Figure 41. Kinetic energy profiles at selected spanwise locations in the downstream plane at $x/h = 3.69$ for 3D hill flow..

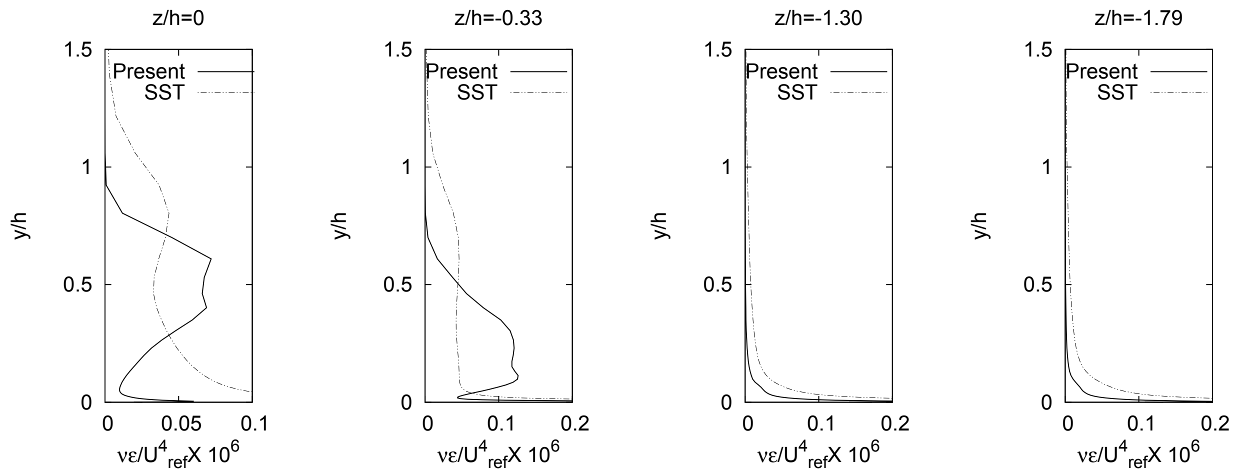

Figure 42. Dissipation-rate profiles at selected spanwise locations in the downstream plane at $x/h = 3.69$ for 3D hill flow..

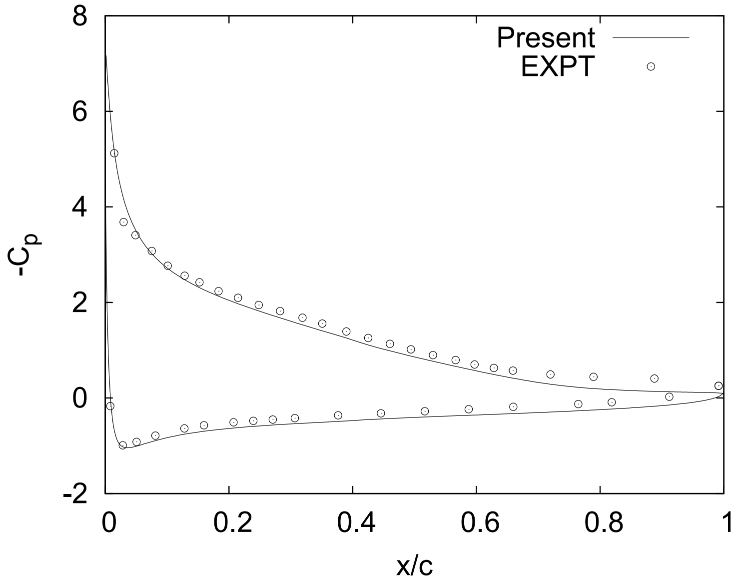

Figure 43. Pressure coefficients along NACA4412 surface.

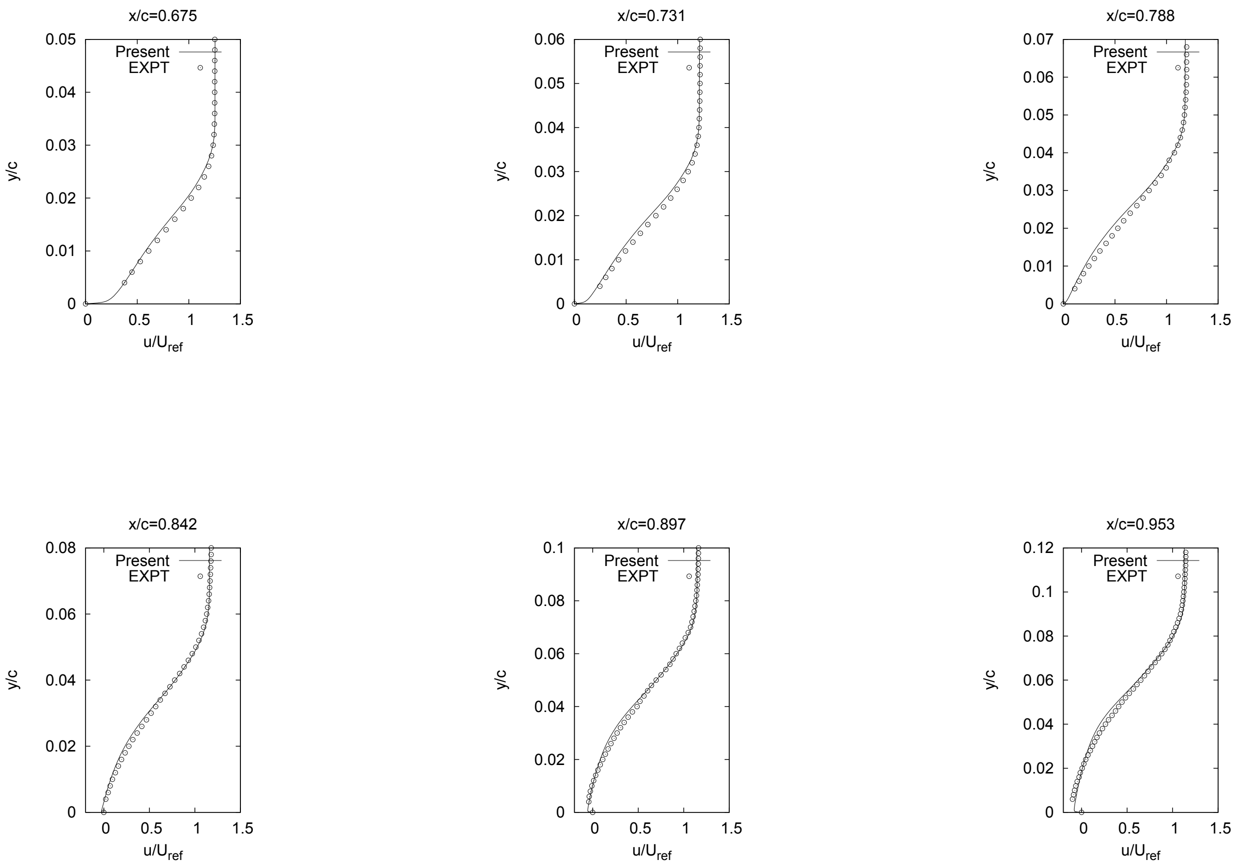

Figure 44. Mean streamwise velocity profiles near separation edge of NACA4412.

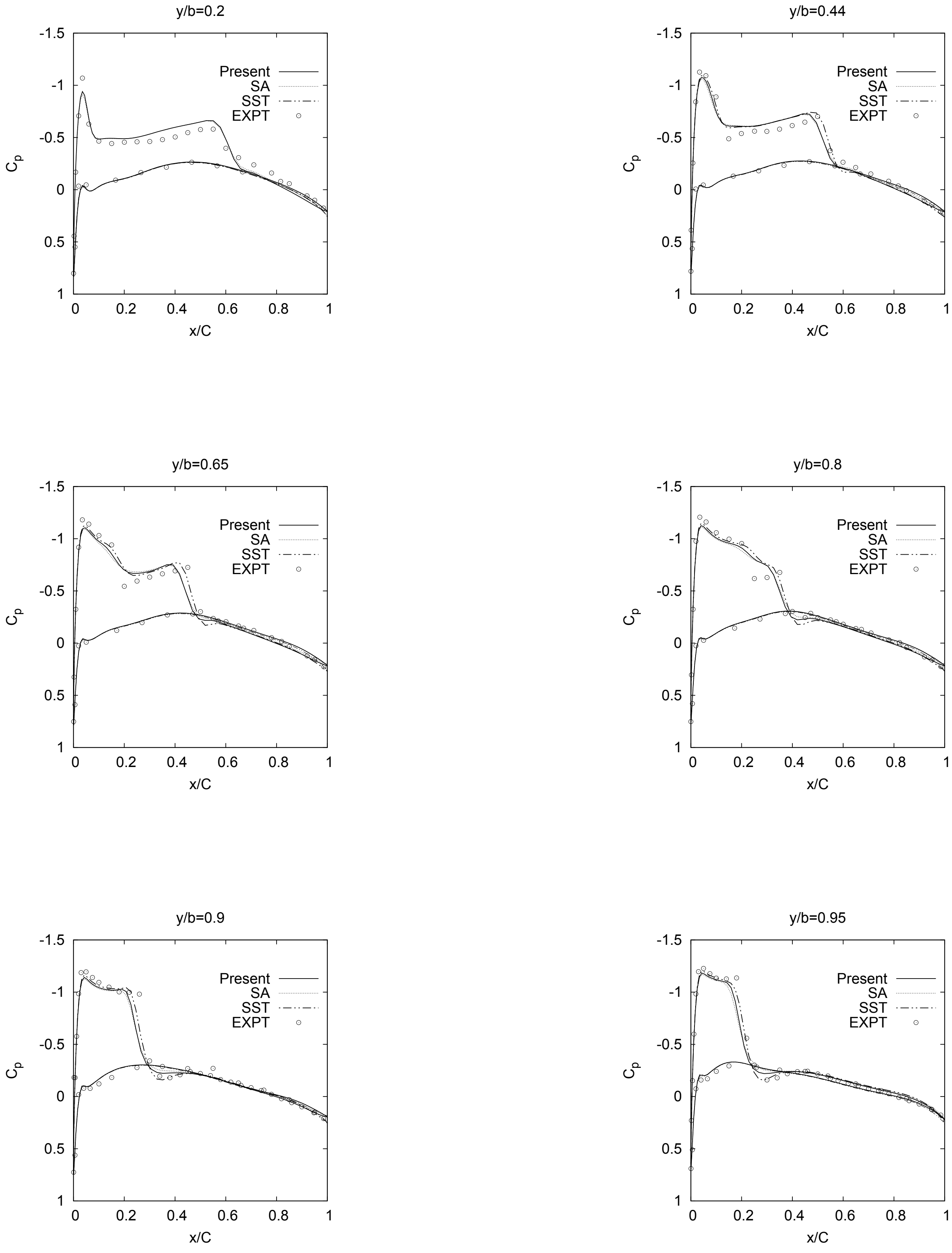

Figure 45. Wall–pressure coefficients at selected cross sections of ONERA–M6 wing.

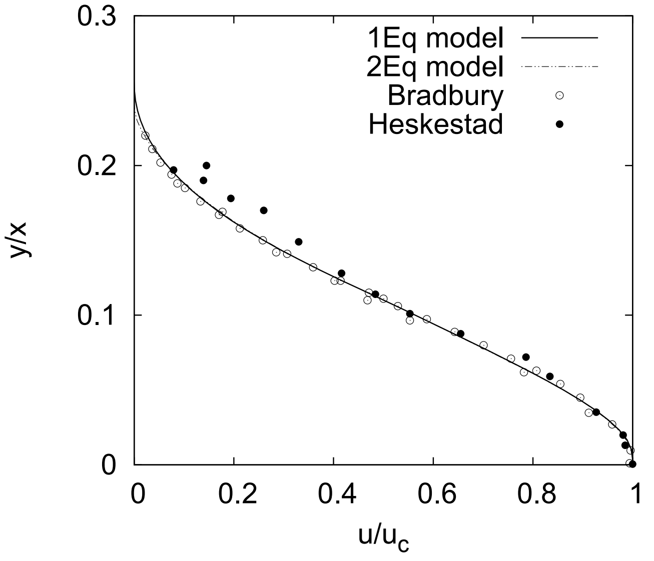

Figure 46. Comparison of computed and measured velocity profiles for plane jet.

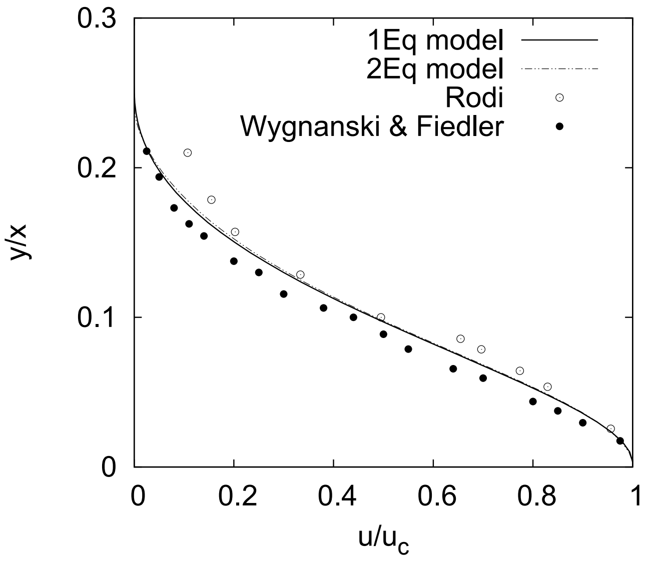

Figure 47. Comparison of computed and measured velocity profiles for round jet.